Measurement, Simulation, and Design of the Dispersion-Engineered Traveling-Wave Kinetic Inductance Amplifier

Senior Thesis Presented by

Saptarshi Chaudhuri

California Institute of Technology

Department of Physics

Advisor: Jonas Zmuidzinas

Submitted May 7, 2013

ABSTRACT

Recently, *Eom et al.* [1] proposed a new concept for a low-noise cryogenic amplifier known as a Dispersion-Engineered Traveling-Wave Kinetic Inductance (DTWKI) amplifier. This device exploits the nonlinear kinetic inductance of superconducting thin-film nitrides to achieve high gain-bandwidth, near quantum-limited noise, and excellent dynamic range. In this thesis, we describe recent progress toward an experimental realization of the DTWKI; in particular, we focus on improvements in the areas of gain-bandwidth and noise performance. We describe a numerical model of the amplifier, and use this model to interpret experimental results and provide insight into the effects of dispersion-engineering on gain processes. Lastly, based on experimental results and model output, we propose some improvements to the DTWKI device.

ACKNOWLEDGMENTS

First and foremost, I would like to thank my advisor Professor Jonas Zmuidzinas for the opportunity to work on the DTWKI project. I joined his group two and a half years ago, looking to solve some challenging physics problems, and I have been able to do precisely that. Jonas' guidance has been invaluable. Almost every conversation that I have had with him has led to big progress on my work. I would also like to thank my co-mentor Dr. Peter Day of Caltech/NASA Jet Propulsion Laboratory (JPL). His in-depth understanding of both theory and experiment has been critical to the completion of my thesis. I would like to thank Dr. Byeong Ho Eom of JPL, who taught me how to use the microwave measurement equipment and assisted me in measurements. I would also like to thank Dr. Jiansong Gao at the Boulder branch of the National Institute of Standards and Technology (NIST). Our conversations have led to the development of new and exciting devices.

CONTENTS

I. Introduction 1

II. Amplifier Models 10

A. Coupled-Mode Equations 10

B. Harmonic Balance Model 14

1. Modeling A Short Transmission Line Section 15

2. Cascading Transmission Line Sections And Modeling Impedance Changes 20

3. Signal Analysis in a Short Transmission Line Section 25

4. Signal Analysis in a Cascade of Short Transmission Lines 29

III. Gain and Power-Dependent Phase Processes Observed in the DTWKI Amplifier 31

A. Device I 31

B. Device II 45

IV. Noise in the DTWKI Amplifier 53

V. A Proposal For A New DTWKI Design And Looking Forward 59

VI. Appendix 61

A. Computation of Jacobian for Harmonic Balance Model 61

References 63

I. INTRODUCTION

In recent years, there has been increasing demand from the astronomy community for sensitive amplifiers that operate in the microwave, millimeter-wave, and submillimeter-wave bands. To this end, *Eom et al.* have proposed a new concept for a superconducting amplifier known as a Dispersion-Engineered Traveling-Wave Kinetic Inductance (DTWKI) amplifier. [1] Characteristics of the proposed device include:

- Low noise. In theory, the amplifier should operate close to the noise limit imposed by quantum mechanics. Current low-noise transistor amplifiers add noise that is at least a factor of 20 above this limit.

- Large gain-bandwidth. Preliminary model results show that for amplifiers operating under 10 GHz, significant gain can be achieved over a range of 6 GHz. This quality has only been achieved by transistor amplifiers.

- Large dynamic range. High-power signals can be amplified with little distortion. Output saturation levels of -10 dBm or larger are possible. For a gain of 20 dB, this corresponds to an input power of -30 dBm. The dynamic range is far better than that in resonant Josephson parametric amplifiers (JPAs), in which dynamic range is limited by the fact that the internal current is larger than the input-output current by a factor of $\sqrt{Q}$, where Q is the quality factor.

- Low power dissipation. As discussed below, the amplifier requires a strong pump to operate, but only a small fraction of this pump power is dissipated in the device.

- Easy production. The superconducting components of the amplifier can be fabricated through standard thin-film deposition and lithography techniques. So far, all devices have been single layer.

The DTWKI amplifier, if produced as proposed, will have considerable impact in fields (other than astronomy) where detector sensitivity is crucial, including superconducting-detector readout, fundamental physics experiments, quantum information, and low-temperature physics.

As will be discussed below, the DTWKI amplifier falls into the larger class of traveling-wave parametric amplifiers. Parametric amplifiers are so known because the nonlinearity of

the circuit material enables one of the circuit parameters to be varied periodically through the application of a strong pump waveform. If a weak signal waveform is also injected into the device, the periodic variation will transfer power from the pump to the signal, producing significant power gain. The parametric amplification process also generates a waveform of a third frequency, known as the idler. For parametric amplifiers, such as the DTWKI, that are described by four-wave mixing processes (processes discussed in the next chapter), we can write the relationship between the pump f_p, signal f_s, and idler f_i frequencies as $f_i = 2f_p - f_s$.

In the case of the DTWKI device, the varying circuit parameter is the kinetic inductance of the component superconducting thin films. Kinetic inductance is a phenomenon in which the kinetic energy of the Cooper pairs (the particles that carry the current in the superconductor) manifests itself as a surface inductance. The Ginzburg-Landau and BCS theories of superconductivity predict that this inductance varies with the supercurrent.[2] In particular, the second-order Taylor expansion of kinetic inductance, as a function of current, takes the form

$$L(I) = L_0 \left(1 + \frac{I^2}{I_*^2}\right) \tag{1}$$

I_* describes the strength of the nonlinearity. In this thesis, we will refer to L_0 as the characteristic inductance. The lack of a linear term in the expansion can be explained on physical grounds. If a linear term was present, that would imply that the inductance depends on the sign of the current; such behavior is not representative of a physical process.

The impetus behind the development of the DTWKI amplifier is recent advances in the knowledge of superconducting thin-film nitrides. It has been found that titanium nitride (TiN) and niobium titanium nitride (NbTiN) have favorable properties for use in parametric amplifiers. For example, the materials' high normal-state resistivity results in high inductance nonlinearity, which is needed to produce adequate signal power gain. Indeed, recent experiments involving nonlinear resonators show that the inductance modulation can be as high as 8%. Additionally, thin-film nitrides exhibit low power dissipation at the microwave frequencies, which translates into excellent noise performance and allows gain to overcome loss. [3]

Consider a dispersionless superconducting transmission line with nonlinear kinetic inductance. Two obstacles prevent its use as a parametric amplifier, one of which is shock front formation.[4] Consider the propagation of the strong pump in the dispersionless line. From

the equation for the voltage across the inductor, $V = L(I)\frac{dI}{dt}$, it is evident that the nonlinearity will result in generation of the third harmonic frequency $3f_p$. Once the third harmonic is generated, odd higher harmonics $5f_p$, $7f_p$, etc., can be generated. If the input pump power is sufficiently high, sufficient power will be transferred into the higher harmonics, the pump wave will steepen, as illustrated in Fig. 1, and a shock wave will form. Once a shock wave forms, the current in the line exceeds the critical current, and the transmission line becomes resistive. This, in turn, leads to the dissipation of the pump power, inhibiting amplification. We can also think of the shock wave process purely in terms of phase velocity. The current-dependent inductance leads to a current-dependent phase velocity, $v_\phi(I) = \frac{1}{\sqrt{L(I)C}}$. Consequently, points on the wave that correspond to higher currents move more slowly than their lower-current counterparts, causing the wave to steepen as illustrated in Fig. 1. The wave continues to propagate until it becomes nearly infinitely steep, at which point a shock front forms, and as before, efficient amplification is prevented.

Additionally, amplification in the dispersionless nonlinear transmission line is limited by phase mismatch. The principal process for the production of signal gain is the conversion of two pump photons into one signal and one idler photon. The degree to which the phases of the three tones –pump, signal, and idler– are matched determines how coherently the signal is generated along the length of the line, and thus, determines how much gain is generated at the output. This idea will be explored in greater quantitative precision in the next section, but for now, we introduce some terminology that will allow us to understand the concept. The kinetic inductance nonlinearity of (1) results in the pump tone interacting with its own AC current to produce an additional phase shift on the pump. This additional phase shift is known as *self-phase modulation*. There is also an interaction between only the pump and signal that results in an additional phase shift on the signal tone; a similar nonlinear phase shift is also present on the idler tone. These phase shifts are known as *signal cross-phase modulation* and *idler cross-phase modulation*. As discussed in the next section, in all three effects, the phase shift is linear in input pump power and linear in transmission line length.

Let $\theta_p(z)$, $\theta_s(z)$, and $\theta_i(z)$ represent the phase of the pump, signal, and idler tones, as a function of position along the transmission line; let $\Delta\psi(z) = \theta_s(z) + \theta_i(z) - 2\theta_p(z)$ represent the phase difference between the tones. (The factor of 2 takes into account the fact that a signal and idler photon pair is the result of an interaction between *two* pump photons.) In the situation that no idler is present at the input, as in the DTWKI, the closer this phase

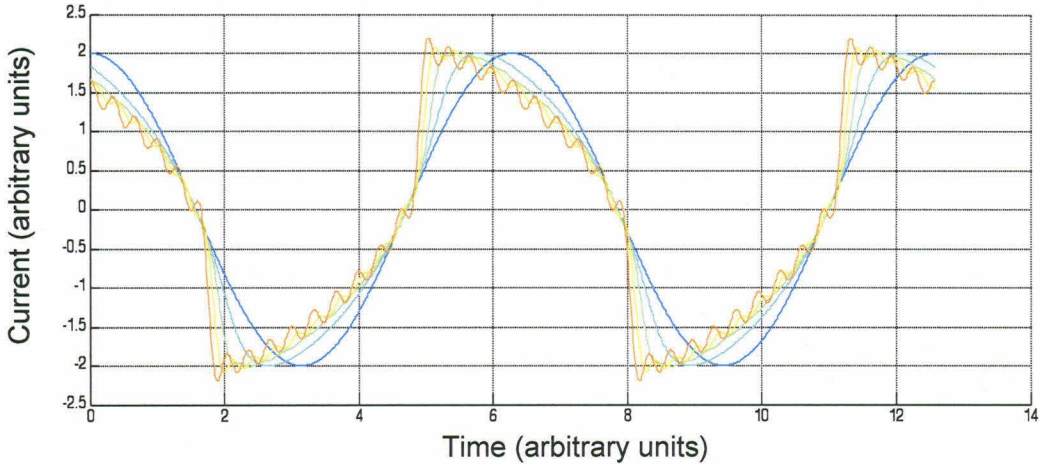

FIG. 1. Illustration of shock wave formation in a transmission line with kinetic inductance nonlinearity given by (1). The dark blue curve represents the time-domain pump waveform at the input. The phase velocity $v_\phi = \frac{1}{\sqrt{L(I)C}}$ decreases as the magnitude of current increases; the higher-magnitude current values propagate more slowly compared to the lower-magnitude current values. As a result, the input waveform steepens, resulting in the time-domain waveform represented by the light blue curve at a position further along the line in the direction of propagation. The wave continues to steepen as it propagates further down the line (green, yellow curves) until it becomes infinitely steep (red curve). At this point, a shock wave forms, and the power in the pump is dissipated.

difference remains to $\Delta\psi(z=0)$ as the wave propagates down the line, the higher the gain is. The coupled-mode equations, discussed in the next section, predict that in a dispersionless transmission line of length L, the above phase modulation effects produce a phase slippage between the three tones, $\Delta\psi(z) \neq \Delta\psi(0)$, resulting in signal and idler power gains of

$$G_s \approx 1 + (L\Delta\phi)^2 \tag{2}$$

$$G_i \approx (L\Delta\phi)^2 \tag{3}$$

for signal frequencies near the pump. Here, $\Delta\phi$ is the pump self-phase modulation per unit length. We denote the total self-phase shift over the line by $\Delta\theta = L\Delta\phi$. Together with the fact that shock fronts form at phase shift $\Delta\theta \leq 1$, equation (2) implies that the maximum possible gain is a factor of 2, or 3 dB. Such gain is too small for practical applications.

In summary, a dispersionless nonlinear transmission line cannot be used as an amplifier due to shock front formation, which leads to dissipation of pump power, [4] and phase mismatch, which limits the amplifier to a small quadratic gain.

In the DTWKI device, which, in the current generation, is in the form of a distributed-element coplanar waveguide (CPW) consisting of NbTiN thin films, both of these issues are to be resolved through a loading process in which we periodically perturb the center strip width, and hence the impedance, of the transmission line. The loading process is illustrated in Fig. 2 and Fig. 3. Let f_{per} be a frequency that is slightly larger than the third pump harmonic $3f_p$. The center strip width of the CPW is periodically increased (and thus, the impedance decreased), with the separation of perturbations being one-half wavelength corresponding to the frequency f_{per}. Much like an electronic bandgap, this creates a stopband –a range of frequencies that are not transmitted by the transmission line– centered at f_{per} that includes the third harmonic $3f_p$. The stopband limits higher harmonic generation and prevents shock front formation. We also tweak every third loading by reducing its length to half the length of the first two loadings. This creates weaker stopbands at $f_{per}/3$ and $2f_{per}/3$ and results in dispersion features near these frequencies. By fine-tuning the pump frequency near the stopband at $f_{per}/3$, this dispersion can be used to compensate for nonlinear phase slippage. As a result, the phases of the three tones can be matched ($\Delta\psi(z) = \Delta\psi(0)$ for all z) for a wide range of signal frequencies, and the amplifier can operate in the exponential gain regime:

$$G_s \approx 1 + \sinh^2(L\Delta\phi) \tag{4}$$

$$G_i \approx \sinh^2(L\Delta\phi) \tag{5}$$

for signal frequencies over a wide bandwidth around the pump. To see the vast improvement given by this dispersion engineering, consider the application of a strong pump that produces a self-phase shift of $\Delta\theta = 3$ at the output of the amplifier. In the quadratic gain regime, assuming shock wave formation does not occur (i.e. the third harmonic falls in a stopband), the signal gain is a factor of 10, or 10 dB, whereas in the exponential gain regime, the signal gain is approximately a factor of 100, or 20 dB.

In addition to the exponential wideband gain, another attractive feature of the DTWKI amplifier is near quantum-limited noise. The DTWKI belongs to the class of phase-insensitive amplifiers, so known because both quadratures of the signal are amplified equally.

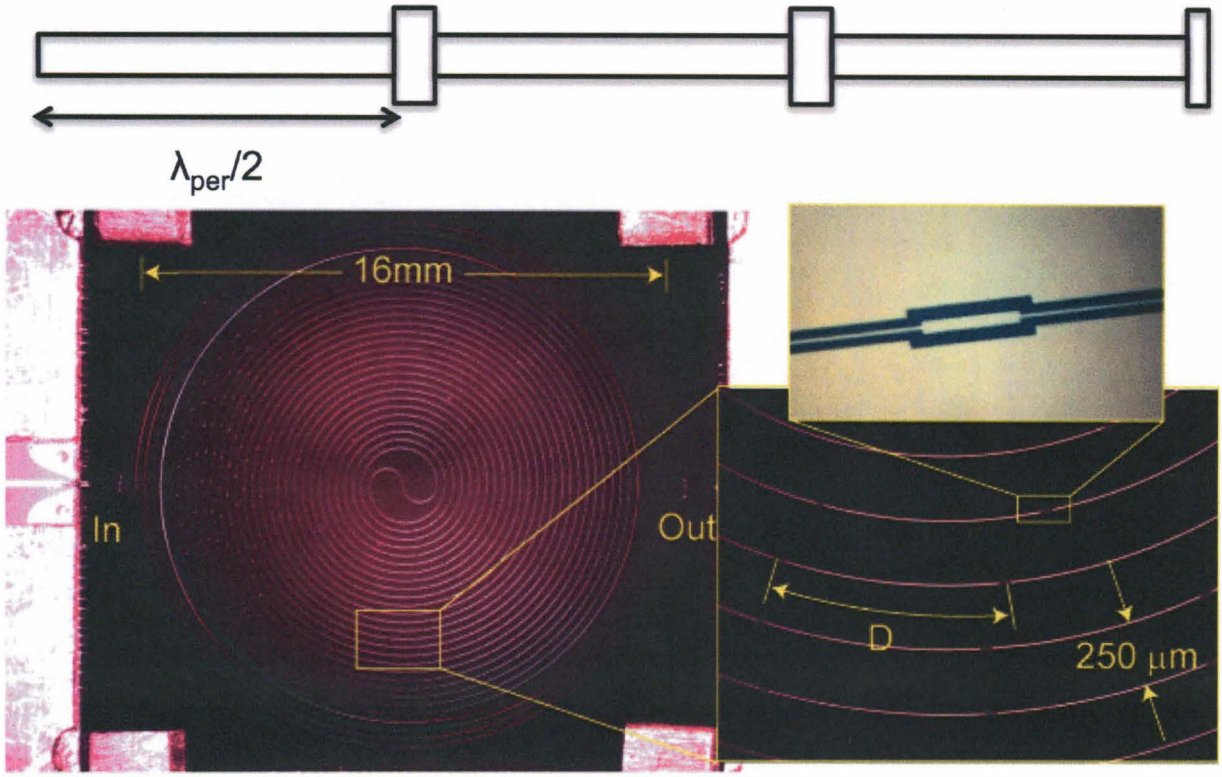

FIG. 2. **Top**: A schematic of the periodic structure of the center strip in the DTWKI amplifier. The introduction of a wide section every 1/2 wavelengths at frequency f_{per} inhibits higher harmonic generation, while reducing the length of every third loading introduces the dispersion at the pump needed for phase matching and exponential gain. **Bottom**: An image of an early DTWKI test sample, fabricated in the form of a CPW from NbTiN thin films, which illustrates the loading process. The transmission line is in the form of a double-spiral coplanar waveguide, with the input and output ports as labelled above. The length of the amplification section is 0.6 meters, which is approximately 225 wavelengths at the pump frequency 11.56 GHz. At each end of the amplification section is a 0.1-meter turn of impedance taper, which has impedance of nearly 300 ohms at the intersection with the amplification section and an impedance of 50 ohms at the port. Every $D = 877$ μm, the center strip width is increased by a factor of three, as illustrated in the top right panel. The length of the first two loadings in the six-section periodic structure is 50 μm, while the length of the third loading is 25 μm. The impedance of these wider sections is approximately two-fifths that of the rest of the line. The distance between adjacent turns of the spiral is 250 μm; the large spacing minimizes coupling between the adjacent turns.

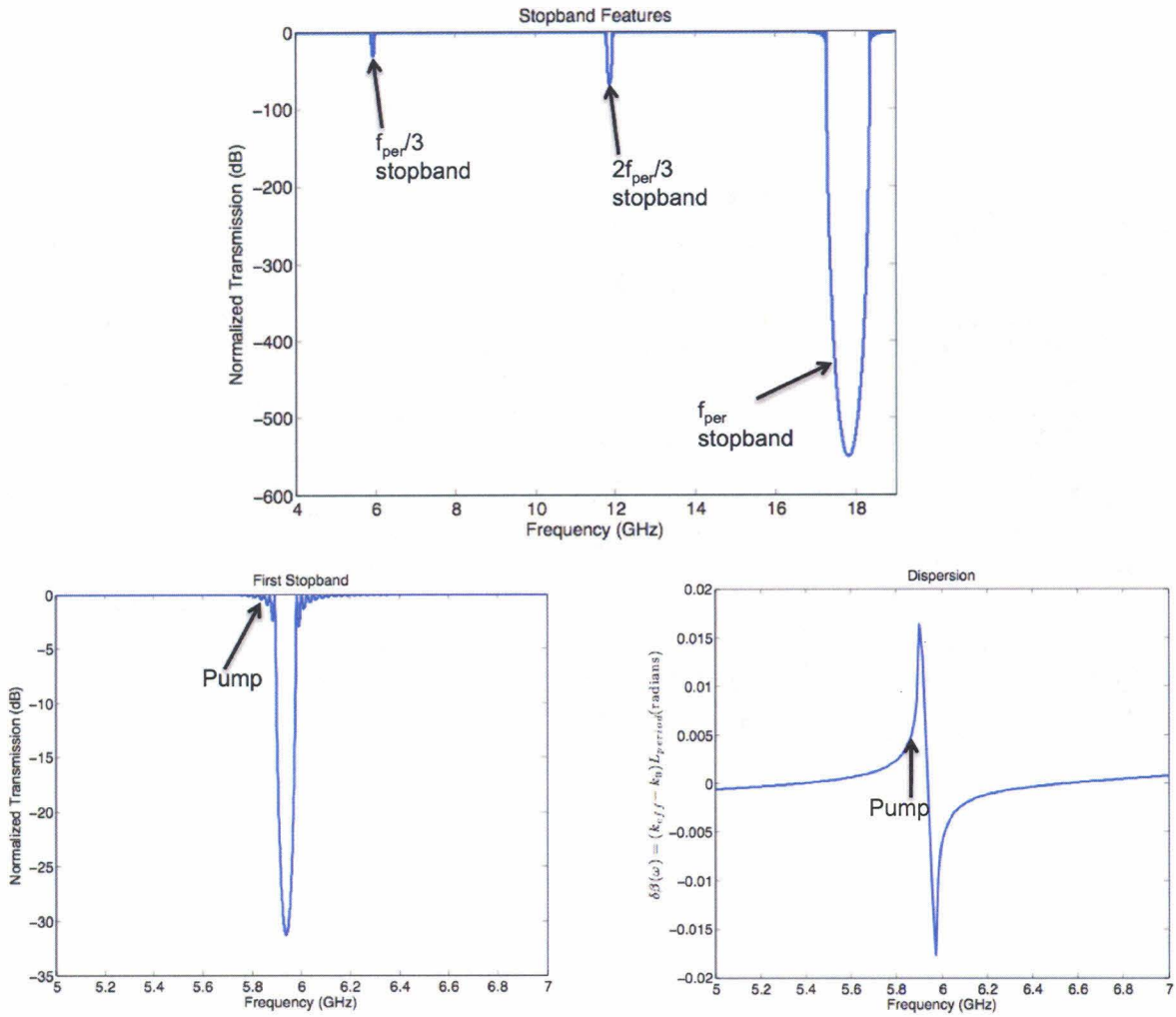

FIG. 3. **Top**: A schematic of the stopbands created at $f_{per}/3$, $2f_{per}/3$, and f_{per} by the loading process. Here, the stopbands are centered near 6, 12, and 18 GHz. **Bottom Left**: A magnified view of the stopband near 6 GHz, showing an example pump frequency. **Bottom Right**: The dispersion associated with the $f_{per}/3$ stopband, showing the location of the pump chosen in the figure to the left. k_{eff} is the effective wavenumber in the presence of dispersion and k_0 is the wavenumber in the absence of dispersion. The y-axis represents the contribution of dispersion to the phase shift of a wave traveling through a six-block periodic structure.

The uncertainty principle from quantum mechanics asserts that, for this class of amplifiers, there is a fundamental lower-limit on the fluctuations of the signal quadrature components added by amplification. This fundamental lower-limit, called the standard quantum limit, or SQL, is one-half of a photon per second per unit bandwidth. Adding the one-half-photon

vacuum noise yields the quantum-limit noise temperature of $T_{SQL} = \frac{hf}{k_B} = f \times 48$ mK/GHz, where h is Planck's constant and k_B is Boltzmann's constant. In theory, the DTWKI should be able to achieve such quantum-limited noise; the amplifier need not add thermal noise or shot noise. [5] In contrast, state-of-the-art high electron mobility transistors (HEMTs) possess noise temperature above 1 K/GHz, corresponding to an added noise of at least 20 photons.

In parametric amplifiers based on Josephson junctions, it has been demonstrated that the fluctuations of one quadrature component can be reduced below the quantum limit at the expense of increasing fluctuations in the other quadrature, a phenomenon known as squeezing. [6] The DTWKI is a non-degenerate parametric amplifier, as the signal is generally far away from the pump frequency. In this case, the fluctuations of the amplified signal quadratures will be equal, but will be highly correlated with fluctuations at the idler frequency. This phenomenon, known as two-mode squeezing, has many potential applications in quantum information science.

Lastly, it is important to note that several amplifiers based on principles similar to those described above have already been demonstrated, illustrating the feasibility of producing the DTWKI amplifier. For example, narrowband resonator-based parametric amplifiers using nonlinear kinetic inductance have been demonstrated by *Tholen et al.*[7] In 1967, an optical traveling-wave parametric amplifier that makes use the Kerr nonlinearity of optical fibers -in which the index of refraction is intensity-dependent- was patented.[8] The latter is of special significance, as in theory, the transmission line structure of the DTWKI device should work in a manner similar to that of the optical fiber.

In Chapter 2, Section A, of this thesis, we discuss the coupled-mode equations, a simple, analytical framework for discussing traveling-wave amplifiers which is borrowed from the field of nonlinear optics. In Chapter 2, Section B, we discuss a harmonic balance model which is designed to capture physics associated with the formation of standing waves that is not captured in the coupled-mode equations.

In Chapter 3, we discuss experimental results concerning gain processes in the DTWKI. By comparing the experimental data with the model output, we explore the physics behind deamplification, in which the gain is less than 1, and the reduction of gain due to mixing processes involving sidebands of higher harmonics. We also discuss the causes and consequences of impedance mismatch between the taper and the amplifier.

In Chapter 4, we discuss the experimental noise performance of recent DTWKI samples. We discuss progress toward achieving quantum-limited noise and in particular, efforts to reduce on-chip heating.

Finally, in Chapter 5, we propose a design for the next generation of devices that should achieve the best gain-bandwidth and noise performance of any DTWKI to date. We discuss efforts to realize two-mode squeezing, and more broadly, we discuss future plans for DTWKI development. Lastly, we discuss other novel methods for developing low-noise amplifiers.

II. AMPLIFIER MODELS

A. Coupled-Mode Equations

Consider a transmission line of length L, which has some intrinsic dispersion. By "intrinsic", we mean that the dispersion is caused by some effect that occurs everywhere on the line and thus, that the dispersion affects the phase evolution of a monochromatic waveform on a per unit length basis. By using this model, we assume that the dispersion created by the impedance loadings in the DTWKI can be modeled as some effective intrinsic dispersion. The differential equations governing voltage and current on the transmission line are

$$\frac{\partial V}{\partial z} = -L(I)\frac{\partial I}{\partial t} \tag{6}$$

$$\frac{\partial I}{\partial z} = -C\frac{\partial V}{\partial t} \tag{7}$$

where $L(I)$ is the inductance per unit length, given by equation (1), and C is the capacitance per unit length. Combining the two equations, we obtain a wave equation for current:

$$\frac{\partial^2 I}{\partial z^2} - \frac{\partial}{\partial t}\left[L(I)C\frac{\partial I}{\partial t}\right] = 0 \tag{8}$$

We express the current I as the sum of a number of frequency components,

$$I = \frac{1}{2}\left(\sum_n A_n(z)e^{i(k_n z - \omega_n t)} + c.c.\right) \tag{9}$$

where $c.c$ represents the complex conjugate of the first term, and the slowly varying complex amplitudes A_n satisfy

$$\left|\frac{d^2 A_n}{dz^2}\right| \ll \left|k_n \frac{dA_n}{dz}\right| \tag{10}$$

The $I^2 dI/dt$ nonlinearity connects combinations of four frequencies. Thus, a general discussion of four-wave mixing in a Kerr medium includes four frequencies in the sum in (9): two pump tones at ω_{p1} and ω_{p2}, a signal at ω_s, and a generated idler at $\omega_i = \omega_{p1} + \omega_{p2} - \omega_s$. In degenerate four-wave mixing, the two pump tones are at the same frequency, $\omega_p = \omega_{p1} = \omega_{p2}$. Plugging the expansion (9) into (8) and using the approximation in (10), the evolution of the amplitudes A_p, A_s, and A_i is governed by the following coupled-mode equations [9]:

$$\frac{dA_p}{dz} = \frac{i\omega_p}{8\bar{c}I_*^2}\left[(|A_p|^2 + 2|A_s|^2 + 2|A_i|^2)A_p + 2A_s A_i A_p^* \exp(i\Delta\beta z)\right]$$

$$\frac{dA_s}{dz} = \frac{i\omega_s}{8\bar{c}I_*^2}\left[(|A_s|^2 + 2|A_i|^2 + 2|A_p|^2)A_s + A_i^* A_p^2 \exp(-i\Delta\beta z)\right]$$
$$\frac{dA_i}{dz} = \frac{i\omega_i}{8\bar{c}I_*^2}\left[(|A_i|^2 + 2|A_s|^2 + 2|A_p|^2)A_i + A_s^* A_p^2 \exp(-i\Delta\beta z)\right] \quad . \tag{11}$$

where $\bar{c} = \frac{1}{\sqrt{L_0 C}}$ is a characteristic phase velocity, and $\Delta\beta = k_s + k_i - 2k_p$ is the linear phase mismatch.

From equation (8), it is clear that the pump, signal, and idler are not the only tones traveling in the line. As mentioned before, the four-wave mixing process creates odd pump harmonics $(2n+1)\omega_p$, $n = 1, 2, \ldots$, as well as tones of frequency $(2n+1)\omega_p \pm (\omega_s - \omega_p)$. The latter frequencies are called *sideband frequencies*; the tone below $(2n+1)\omega_p$ is the known as the *lower sideband* of the harmonic, while the tone above $(2n+1)\omega_p$ is known as the *upper sideband* of the harmonic. We could expand (11) to include these modes; for simplicity, here we assume that these higher frequency tones fall in a stopband and do no propagate, or at least, that the dispersion engineering creates a phase mismatch such that the higher frequency tones do not interact coherently with lower frequency tones, in which case the amplitude of the higher frequency tones is negligible compared to those at lower frequency.

In the DTWKI, the signal is typically very weak compared to the pump, so we can drop all terms in equations (11) except those that scale as $|A_p|^2$ or $|A_p|^3$. This approximation is known as the *weak-signal approximation.* We also assume that the pump is undepleted as it travels through the line, so that $d|A_p|/dz = 0$. In this case, the first equation in (11) can be solved for A_p:

$$A_p(z) = A_p(0)\exp\left(\frac{i\omega_p|A_p|^2 z}{8\bar{c}I_*^2}\right) \tag{12}$$

Thus, from (12), we see that the nonlinearity causes an additional phase shift per unit length of

$$\Delta\phi = \frac{\omega_p|A_p|^2}{8\bar{c}I_*^2} \tag{13}$$

This is precisely the self-phase modulation introduced in the previous section. The expression for self-phase modulation can also be derived by extracting the coefficient of A_p from the right-hand side of the dA_p/dz expression in (11). Since $|A_p|^2 \propto P_{in}$, where P_{in} is the input pump power, we see that the self-phase modulation is linear in input power, as mentioned in the Introduction.

Plugging (12) into the differential equations (11) (after applying the weak signal approximation) and using the methods explained in [10] yields analytical solutions for the signal

and idler amplitude

$$A_s(z) = A_s(0)\exp\left(i\left(\frac{2\omega_s}{\omega_p}\Delta\phi - \frac{\kappa}{2}\right)z\right)\left(\cosh(gz) + \frac{i\kappa}{2g}\sinh(gz)\right) \tag{14}$$

$$A_i(z) = A_s(0)\exp\left(i\left(\frac{2\omega_i}{\omega_p}\Delta\phi - \frac{\kappa}{2}\right)z\right)\left(\frac{i\Delta\phi}{g}\frac{\omega_i}{\omega_p}\sinh(gz)\right) \tag{15}$$

where $\kappa = \Delta\beta + 2\Delta\phi$ and g is the parametric gain coefficient, given by

$$g = \frac{1}{2}\sqrt{\frac{\omega_s\omega_i}{\omega_p^2}(2\Delta\phi)^2 - \kappa^2} \tag{16}$$

In deriving equations (14) and (15), we have assumed that no idler is present at the input $z = 0$. (No idler is excited at the input in experiment, making this an appropriate assumption.)

From analyzing the complex exponent in the solutions (14) and (15) or by extracting the coefficient of A_s and A_i in (11), the signal and idler cross-phase modulation per unit length is found:

$$\begin{aligned}\Delta\phi_s &= \frac{2\omega_s|A_p|^2}{8\bar{c}I_*^2} = \frac{2\omega_s}{\omega_p}\Delta\phi \\ \Delta\phi_i &= \frac{2\omega_i|A_p|^2}{8\bar{c}I_*^2} = \frac{2\omega_i}{\omega_p}\Delta\phi\end{aligned} \tag{17}$$

Note that the $\frac{\kappa}{2}$ term from the complex exponent in (14) and (15) is not present in (17). The reason for this is that the κ phase term is the result of the interaction of three tones– specifically, the conversion of two pump photons into signal and ider photons; cross-phase modulation is a result of interactions between only two tones– either the pump and the signal or the pump and the idler.

With no dispersion, $\Delta\beta = 0$, and from (12), (14), (15), the pump, signal, and idler are not phase-matched:

$$\Delta\psi(z) = \Delta\psi(0) + \arctan\left(\frac{1}{\left|1 - \frac{\omega_s}{\omega_p}\right|}\tan\left(\Delta\phi\left|1 - \frac{\omega_s}{\omega_p}\right|z\right)\right) \tag{18}$$

The signal and idler power gains are

$$G_s(\omega_s) = \frac{|A_s(L)|^2}{|A_s(0)|^2} = 1 + \left(\frac{1}{\left|1 - \frac{\omega_s}{\omega_p}\right|^2} - 1\right)\sin\left(\left|1 - \frac{\omega_s}{\omega_p}\right|L\Delta\phi\right)^2 \tag{19}$$

$$G_i(\omega_i) = \frac{|A_i(L)|^2}{|A_s(0)|^2} = \frac{1}{\left|1 - \frac{\omega_i}{\omega_p}\right|^2}\left(\frac{\omega_i}{\omega_p}\right)^2\sin\left(\left|1 - \frac{\omega_i}{\omega_p}\right|L\Delta\phi\right)^2 \tag{20}$$

Taking the limit $\omega_s \to \omega_p$, we recover the quadratic gain results of (2) and (3).

From (16), the parametric gain coefficient is maximized when $\kappa = 0$. It is easy to see that this condition corresponds to the pump, signal, and idler being phase-matched. The signal and idler power gains are

$$G_s(\omega_s) = 1 + \sinh\left(\sqrt{\frac{\omega_s\omega_i}{\omega_p^2}}L\Delta\phi\right)^2 \tag{21}$$

$$G_i(\omega_i) = \frac{\omega_i}{\omega_s}\sinh\left(\sqrt{\frac{\omega_s\omega_i}{\omega_p^2}}L\Delta\phi\right)^2 \tag{22}$$

Taking the limit $\omega_s \to \omega_p$, we recover the exponential gain results of (4) and (5).

The phase-matching condition can be written as

$$\Delta\beta = k_s + k_i - 2k_p = -2\Delta\phi \tag{23}$$

To achieve this condition, we can modify the dispersion in the region of the signal. However, this achieves exponential gain only in a narrow section around the signal. If we instead modify the dispersion at the pump (and add no dispersion at the signal or idler), we achieve this phase-matching condition, and consequently, exponential gain, for a wide range of signal frequencies. As illustrated in Fig. 3, the periodic structure in the DTWKI accomplishes the task of producing dispersion in a narrow range of frequencies around the pump.

To illustrate the enhanced gain-bandwidth provided by dispersion engineering, we plot the signal gain for various levels of phase mismatch in Fig. 4. For the transmission line with no dispersion engineering, described by the $\Delta\beta = 0$ curve, the peak gain is 10 dB, with the boundaries of the 3 dB bandwidth occurring at $\frac{f_s}{f_p} = 0.566$ and $\frac{f_s}{f_p} = 1.434$. This yields a bandwidth of $B = 0.866$. For the $\Delta\beta = -\Delta\phi$ curve, which describes a transmission line that is dispersion-engineered but not phase-matched, the peak gain is 17.82 dB, with the boundaries of the 3 dB bandwidth occurring at $\frac{f_s}{f_p} = 0.541$ and $\frac{f_s}{f_p} = 1.459$. This yields a bandwidth of $B = 0.918$. For the $\Delta\beta = -2\Delta\phi$ curve, which describes a phase-matched transmission line, the peak gain is 20.06 dB, with the boundaries of the 3 dB bandwidth occurring at $\frac{f_s}{f_p} = 0.532$ and $\frac{f_s}{f_p} = 1.468$. This yields a bandwidth of $B = 0.936$. Thus, by using dispersion engineering, we increase the peak signal gain by a factor of 10 and the bandwidth by approximately 8%.

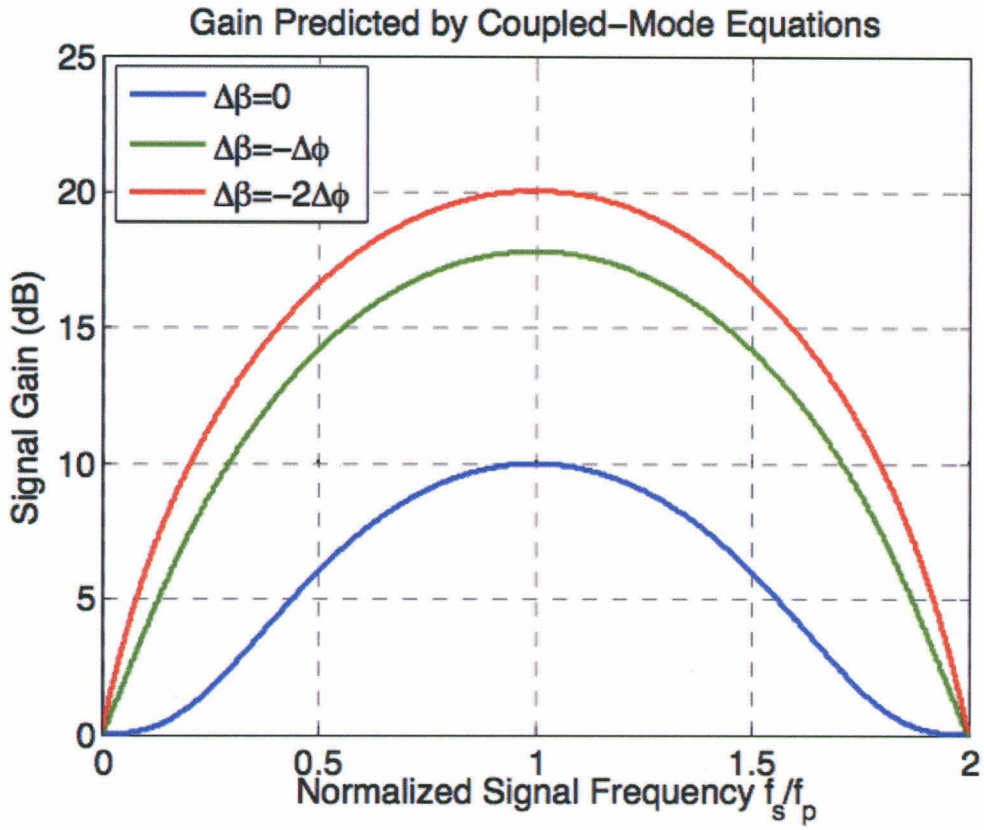

FIG. 4. The gain predicted at self-phase shift $\Delta\theta = L\Delta\phi = 3$ for varying levels of linear phase mismatch. The signal frequency is normalized by the pump frequency. Note that both the gain and the bandwidth increase as the degree of phase mismatch decreases.

B. Harmonic Balance Model

Though the coupled-mode equations provide us with a simple way to understand the physics of the DTWKI, it has significant shortcomings. The impedance steps in the device produce reflections, which in turn, create standing waves. Consequently, the current amplitude varies with position on the line, and if the degree of variation is not sufficiently small, the approximation $d|A_p|/dz = 0$ used in solving the coupled-mode equations is not valid. Additionally, it is unclear whether we can assume that the dispersion created by the impedance loadings can be treated as an effective intrinsic dispersion. We also may not be able to assume that the power in the higher harmonics and the sidebands of the higher harmonics is insignificant compared to that in the pump, signal, and idler tones. To resolve these issues, we have developed what is known in the electrical engineering community as

a harmonic balance computation scheme. In this treatment, the DTWKI amplifier will be treated as a cascade of weakly nonlinear transmission line sections. Our strategy for determining the nature of pump and signal propagation will be similar to that used in analyzing the coupled-mode equations. We will first solve for the amplitudes of the pump tone and its harmonics throughout the line. Using the solution for the pump tone and the weak-signal approximation, we will then solve for sideband amplitudes, including those of the signal and idler.

1. *Modeling A Short Transmission Line Section*

First, we consider a short transmission line section. This section can be characterized by its length L, its characteristic impedance $Z_c = \sqrt{\frac{L_0}{C}}$, its phase velocity $\bar{c} = \frac{1}{\sqrt{L_0 C}}$ in the limit of zero current, and its I_* value, which, as mentioned before, sets the scale for the nonlinearity. Each section obeys the differential equations (6) and (7). We define the forward and backward-propagating waves in each section as:

$$a(z,t) = \frac{V(z,t) + Z_c I(z,t)}{2\sqrt{Z_c}} \tag{24}$$

$$b(z,t) = \frac{V(z,t) - Z_c I(z,t)}{2\sqrt{Z_c}} \tag{25}$$

Both of these waveforms have dimensions of Watts$^{1/2}$. Substituting these expressions into (6) and (7), we find that these $a(z,t)$ and $b(z,t)$ obey the nonlinear wave equations

$$\frac{\partial a}{\partial z} = -\frac{1}{\bar{c}}\left(\frac{\partial a}{\partial t} + \frac{1}{6I_*^2 Z_c}\frac{\partial}{\partial t}(a-b)^3\right) \tag{26}$$

$$\frac{\partial b}{\partial z} = -\frac{1}{\bar{c}}\left(-\frac{\partial b}{\partial t} + \frac{1}{6I_*^2 Z_c}\frac{\partial}{\partial t}(a-b)^3\right) \tag{27}$$

Under the weak-signal approximation, which allows us to ignore tones that result solely from the mixing of two or more sideband photons, we can decompose $a(z,t)$ and $b(z,t)$ into a sum of pump harmonic and sideband waveforms:

$$a(z,t) = Re\left(\sum_{n=1}^{\infty} a(n\omega_p; z)e^{in\omega_p t} + \sum_{n=-\infty}^{\infty} a(\omega_m; z)e^{i\omega_n t}\right) \tag{28}$$

$$b(z,t) = Re\left(\sum_{n=1}^{\infty} b(n\omega_p; z)e^{in\omega_p t} + \sum_{n=-\infty}^{\infty} b(\omega_m; z)e^{i\omega_n t}\right)$$

(29)

where $\omega_n = n\omega_p + \omega_s - \omega_p$ are the sideband frquencies. In the case that $\omega_n < 0$, the physical frequency of the waveform is $-\omega_n$. In this notation, ω_1 represents the signal frequency, while ω_{-1} represents the idler frequency.

We treat each transmission line section as a two-port circuit, as shown in Fig. 5. a_1 represents a forward-traveling incoming wave at Port 1. It travels through the transmission line section and exits through Port 2. This outgoing wave is represented by b_2. Similarly, a_2 represents a backward-traveling incoming wave at Port 2. It travels through the transmission line section and exits through Port 1. This outgoing wave is represented by b_1.

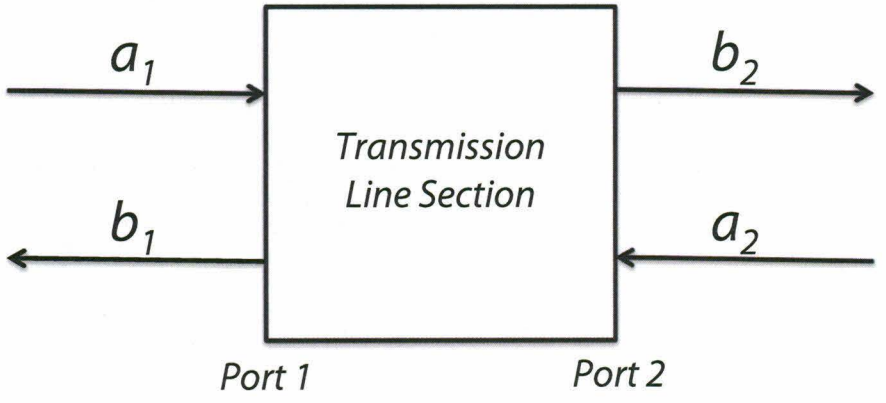

FIG. 5. Here, we show a schematic of a transmission line section. a_1 and a_2 represent, respectively, the forward- and backward-propagating incoming waves , while b_1 and b_2 represent forward- and backward-propagating outgoing waves.

We restrict our attention to propagation of the pump tone and its harmonics. Define $a_1(n\omega_p)$ as the the complex amplitude of the component of the incoming wave a_1 that is at frequency $n\omega_p$. Similarly, define $a_2(n\omega_p)$, $b_1(n\omega_p)$, and $b_2(n\omega_p)$. In the language of equation (28), $a_1(n\omega_p) = a(n\omega_p; z = 0)$, $a_2(n\omega_p) = b(n\omega_p; z = L)$, $b_1(n\omega_p) = b(n\omega_p; z = 0)$, $b_2(n\omega_p) = a(n\omega_p; z = L)$.

We can write the outgoing wave amplitudes at the nth harmonic as a sum of linear and nonlinear contributions from the incoming wave amplitudes:

$$\begin{bmatrix} b_1(n\omega_p) \\ b_2(n\omega_p) \end{bmatrix} = S(n\omega_p) \begin{bmatrix} a_1(n\omega_p) \\ a_2(n\omega_p) \end{bmatrix} + \begin{bmatrix} c_1(n\omega_p) \\ c_2(n\omega_p) \end{bmatrix} \tag{30}$$

where, letting $\bar{c}$ be the section's phase velocity and $k_p = \frac{\omega_p}{\bar{c}}$ be the propagation constant,

$$S(n\omega_p) = \begin{bmatrix} e^{-ink_pL} & 0 \\ 0 & e^{-ink_pL} \end{bmatrix} \tag{31}$$

$S(n\omega_p)$ is a scattering matrix representing a phase shift on the incoming waves due to the traveling waves propagating some nonzero distance. The nonlinear term, represented by the rightmost vector in (30), can be approximated by plugging the expansion of pump harmonics from (28) into Eqs. (26)-(27) and using first-order perturbation theory:

$$\begin{aligned} \underline{c}_1(n\omega_p) = \frac{ink_pL}{24I_*^2Z_c} Le^{-ink_pL} \sum_{k,l,m} \delta_{n,k+l+m} [&a_1(k\omega_p)a_1(l\omega_p)a_1(m\omega_p)\text{sinc}(nk_pL) \\ &- 3a_1(k\omega_p)a_1(l\omega_p)a_2(m\omega_p)\text{sinc}((n-m)k_pL) \\ &+ 3a_1(k\omega_p)a_2(l\omega_p)a_2(m\omega_p)\text{sinc}(kk_pL) \\ &- a_2(k\omega_p)a_2(l\omega_p)a_2(m\omega_p)] \end{aligned} \tag{32}$$

$$\begin{aligned} \underline{c}_2(n\omega_p) = -\frac{ink_pL}{24I_*^2Z_c} e^{-ink_pL} \sum_{k,l,m} \delta_{n,k+l+m} [&a_1(k\omega_p)a_1(l\omega_p)a_1(m\omega_p) \\ &- 3a_1(k\omega_p)a_1(l\omega_p)a_2(m\omega_p)\text{sinc}(mk_pL) \\ &+ 3a_1(k\omega_p)a_2(l\omega_p)a_2(m\omega_p)\text{sinc}((n-k)k_pL) \\ &- a_2(k\omega_p)a_2(l\omega_p)a_2(m\omega_p)\text{sinc}(nk_pL)] \end{aligned} \tag{33}$$

Here, k, l, and m range from $-\infty$ to ∞. For $k < 0$, $a_1(k\omega_p)$ is the complex conjugate of $a_1(-k\omega_p)$, i.e. $a_1(k\omega_p) = a_1(-k\omega_p)^*$ (and similarly for $a_2(k\omega_p)$). For $k = 0$, $a_1(k\omega_p) = a_2(k\omega_p) = 0$. These two equations give us several insights into the nature of the nonlinearity:

- In contrast with the linear response, the nonlinear amplitudes depend on both ports' incoming amplitudes.
- The nonlinear response amplitudes for a certain harmonic depend not only on the incoming amplitudes for that harmonic, but also the incoming amplitude for the other harmonics.

- Note that each term in the summand is the product of three incoming amplitudes. This is due to the quadratic form of the inductance in (1) along with the voltage equation $V = LdI/dt$, which together produce a cubic nonlinearity. As a result of this cubic nonlinearity, if only the fundamental harmonic is injected into the transmission line, only odd harmonics will be produced.

- The generation of third harmonic in the presence of a pump waveform can be seen by letting $k = l = m = 1$ in the above formulas.

- To observe the self-phase modulation effect in this perturbative treatment, excite port 1 with only a pump tone, and do not excite port 2. Then,

$$\underline{c}_2(\omega_p) = -\frac{ik_pL}{8I_*^2Z_c}e^{-ik_pL}|a_1(\omega_p)|^2a_1(\omega_p) \tag{34}$$

so

$$b_2(\omega_p) = a_1(\omega_p)e^{-ik_pL}\left(1 - \frac{ik_pL}{8I_*^2Z_c}|a_1(\omega_p)|^2\right) \approx a_1(\omega_p)\exp\left(-ik_pL - \frac{ik_pL}{8I_*^2Z_c}|a_1(\omega_p)|^2\right) \tag{35}$$

This yields a self-phase modulation per unit length of

$$\Delta\phi = \frac{k_p|a_1(\omega_p)|^2}{8I_*^2Z_c} \tag{36}$$

which is the same result as (13) from the coupled-mode theory, except formulated in terms of power instead of current.

Of course, when implementing these equations in a computational setting, we cannot take into account infinitely many frequencies, so we truncate our analysis and the above sums to some harmonic number k_{max}, $-k_{max} < k, l, m < k_{max}$. k_{max} is determined in simulation by looking for the harmonic number above which the amplitudes are insignificant.

Eqs. (32), (33) give an approximate solution to the nonlinear response amplitudes; to improve upon this approximation, we use the fact that a superconducting line is lossless to excellent approximation. In other words, power is conserved and

$$\sum_{k=1}^{k_{max}}\sum_{i=1}^{2}|a_i(k\omega_p)|^2 = \sum_{k=1}^{k_{max}}\sum_{i=1}^{2}|b_i(k\omega_p)|^2 \tag{37}$$

We define a vector of all incoming amplitudes for a fixed section:

$$\mathbf{a}^{(s)} = \begin{bmatrix} a_1^{(s)}(\omega_p) \\ a_2^{(s)}(\omega_p) \\ a_1^{(s)}(2\omega_p) \\ a_2^{(s)}(2\omega_p) \\ . \\ . \\ . \\ a_1^{(s)}(k_{max}\omega_p) \\ a_2^{(s)}(k_{max}\omega_p) \end{bmatrix} \tag{38}$$

where the superscript (s) represents the sth section. We define similar vectors for the outgoing and nonlinear response amplitudes, denoted $\mathbf{b}^{(s)}$ and $\mathbf{c}^{(s)}$. By eq. 30, these vectors obey the relation

$$\mathbf{b}^{(s)} = S^{(s)}\mathbf{a}^{(s)} + \mathbf{c}^{(s)} \tag{39}$$

where

$$S^{(s)} = \oplus_{k=1}^{k_{max}} S^{(s)}(k\omega_p) \tag{40}$$

The nonlinear response vector can be decomposed into the perturbative solution and a power-conserving correction:

$$\mathbf{c}^{(s)} = \underline{\mathbf{c}}^{(s)} + \delta\mathbf{c}^{(s)} \tag{41}$$

From (37), we deduce that $\delta\mathbf{c}^{(s)}$ must obey

$$\begin{aligned} 0 = &\left\langle S^{(s)}\mathbf{a}^{(s)} \middle| \mathbf{c}^{(s)} \right\rangle + \left\langle \mathbf{c}^{(s)} \middle| S^{(s)}\mathbf{a}^{(s)} \right\rangle + \left\langle \mathbf{c}^{(s)} \middle| \mathbf{c}^{(s)} \right\rangle + \left\langle \delta\mathbf{c}^{(s)} \middle| \mathbf{c}^{(s)} \right\rangle \\ &+ \left\langle \mathbf{c}^{(s)} \middle| \delta\mathbf{c}^{(s)} \right\rangle + \left\langle S^{(s)}\mathbf{a}^{(s)} \middle| \delta\mathbf{c}^{(s)} \right\rangle + \left\langle \delta\mathbf{c}^{(s)} \middle| S^{(s)}\mathbf{a}^{(s)} \right\rangle + \left\langle \delta\mathbf{c}^{(s)} \middle| \delta\mathbf{c}^{(s)} \right\rangle \end{aligned} \tag{42}$$

Since the perturbative solution is assumed to be accurate to good approximation, we desire the size of the correction, $\left\langle \delta\mathbf{c}^{(s)} \middle| \delta\mathbf{c}^{(s)} \right\rangle$, to be minimal. Thus, we can solve for the power-conserving correction using Lagrange multiplier minimization, with (42) as the constraint. The result is

$$\delta\mathbf{c}^{(s)} = \left(\sqrt{\frac{\left\langle \mathbf{a}^{(s)} \middle| \mathbf{a}^{(s)} \right\rangle}{\left\langle S^{(s)}\mathbf{a}^{(s)} + \underline{\mathbf{c}}^{(s)} \middle| S^{(s)}\mathbf{a}^{(s)} + \underline{\mathbf{c}}^{(s)} \right\rangle}} - 1 \right) (S^{(s)}\mathbf{a}^{(s)} + \underline{\mathbf{c}}^{(s)}) \tag{43}$$

2. Cascading Transmission Line Sections And Modeling Impedance Changes

Now consider a cascade of short transmission line sections, such as that which makes up the DTWKI device. A schematic of a cascade is shown in Fig. 6.

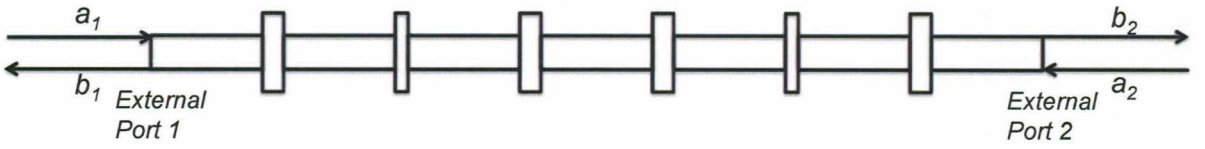

FIG. 6. A schematic of a transmission line cascade. a_1 and a_2 represent the waves excited (i.e. the pump and the signal) at the external ports of the transmission line, while b_1 and b_2 represent the waves leaving the transmission line. The wider sections represent the loadings.

To determine how the pump propagates through the cascade, we must take into account the impedance steps that occur from section to section. Mathematically, this is done by "inserting" impedance-conversion circuits between transmission line sections. We can treat the impedance-conversion circuit as a two-port circuit, as we do with the short transmission line section in Fig. 5. Suppose that a transmission line section has characteristic impedance Z_1 and the adjacent section to the right has characteristic impedance Z_2. Then, for each harmonic, the incoming and outgoing wave amplitudes are related by

$$\begin{bmatrix} b_1(n\omega_p) \\ b_2(n\omega_p) \end{bmatrix} = S(Z_1, Z_2) \begin{bmatrix} a_1(n\omega_p) \\ a_2(n\omega_p) \end{bmatrix} \tag{44}$$

where

$$S(Z_1, Z_2) = \frac{1}{Z_1 + Z_2} \begin{bmatrix} Z_2 - Z_1 & 2\sqrt{Z_1 Z_2} \\ 2\sqrt{Z_1 Z_2} & Z_1 - Z_2 \end{bmatrix} \tag{45}$$

Note that unlike the scattering matrix in Eq. (31), the matrix in (45) depends on impedances, rather than frequency, and thus, it will be the same for all harmonics.

Now we are prepared to solve for the pump and harmonic amplitudes at all ports along

the line. We define a vector of all the incoming amplitudes at every harmonic:

$$\mathbf{a}(k\omega_p) = \begin{bmatrix} a_1^{(1)}(k\omega_p) \\ a_2^{(1)}(k\omega_p) \\ a_1^{(2)}(k\omega_p) \\ a_2^{(2)}(k\omega_p) \\ . \\ . \\ . \\ a_1^{(N)}(k\omega_p) \\ a_2^{(N)}(k\omega_p) \end{bmatrix} \tag{46}$$

Here, N is the total number of sections, including impedance-conversion circuits. Similarly, we can define $\mathbf{b}(k\omega_p)$ and $\mathbf{c}(k\omega_p)$ for the outgoing and nonlinear response amplitudes. Note that for the latter vector, every other pair of entries will be zero because impedance-conversion circuits are linear. We define the total scattering matrix $S(k\omega_p)$ by

$$S(k\omega_p) = \oplus_{s=1}^{N} S^{(s)}(k\omega_p) \tag{47}$$

For odd s, $S^{(s)}(k\omega_p)$ is given by the transmission line scattering matrix in (31), while for even s, it is given by the impedance-conversion matrix in (45).

Additionally, we define an internal projection matrix

$$P_i = \begin{bmatrix} 0 & . & . & . & . & 0 \\ 0 & 1 & 0 & . & . & . \\ . & 0 & 1 & 0 & . & . \\ . & . & . & . & . & . \\ . & . & . & 0 & 1 & 0 \\ 0 & . & . & . & . & 0 \end{bmatrix} \tag{48}$$

and an external projection matrix given by $P_e = 1 - P_i$. These matrices can be interpreted as follows: A vector of the form (46) multiplied by P_e gives the harmonic amplitudes at the external ports, at which the waves are excited. The same vector multiplied by P_i gives the harmonic amplitudes at every internal port –that is, at every port between these external

ports. Finally, we define a connection matrix

$$C = \begin{bmatrix} 0 & . & . & . & . & . & . & 0 \\ . & . & 0 & 1 & . & . & . & . \\ . & . & 1 & 0 & . & . & . & . \\ . & . & . & . & 0 & 1 & . & . \\ . & . & . & . & 1 & 0 & . & . \\ . & . & . & . & . & . & . & . \\ . & . & . & . & . & . & . & . \\ 0 & . & . & . & . & . & . & 0 \end{bmatrix} \tag{49}$$

More explicity, if we let $C_{i,j}$ represent the entry in the ith row and the jth column (starting the indexing at 1), then for $2 \leq n \leq N, C_{2(n-1),2n-1} = 1$ and $C_{2n-1,2(n-1)} = 1$, and $C_{i,j} = 0$ everywhere else. The amplitudes of the outgoing waves of a two-port circuit are equal to the amplitudes of the incoming waves at the adjacent two-port circuits. Mathematically, this can be expressed as

$$P_i \mathbf{a}(k\omega_p) = C\mathbf{b}(k\omega_p) \tag{50}$$

Putting together eq. (30),(46)-(50) gives an expression for the incoming wave amplitudes for internal ports:

$$P_i \mathbf{a}(k\omega_p) = [1 - CS(k\omega_p)]^{-1} C[S(k\omega_p)P_e \mathbf{a}(k\omega_p) + \mathbf{c}(k\omega_p)] \tag{51}$$

where 1 is the $2N \times 2N$ identity matrix. Note that $P_e\mathbf{a}(k\omega_p)$ represents the incoming amplitudes for the external ports for the kth harmonic. These amplitudes can be treated as known parameters in this model, since they are representative of the waveform that we inject into the line. In the current generation of the DTWKI, no pump harmonics are excited at the external ports, so $P_e\mathbf{a}(k\omega_p) = \mathbf{0}$ for $k \neq 1$. Additionally, only one of the ports is excited, so $a_1^{(1)}(\omega_p) \neq 0$, while $a_2^{(N)}(\omega_p) = 0$.

We can combine the equations (51) for each harmonic into one master equation. Let

$$\mathbf{a} = \begin{bmatrix} \mathbf{a}(\omega_p) \\ \mathbf{a}(2\omega_p) \\ \mathbf{a}(3\omega_p) \\ . \\ . \\ . \\ \mathbf{a}(k_{max}\omega_p) \end{bmatrix} \tag{52}$$

Denote its complex conjugate by

$$\mathbf{a}^* = \begin{bmatrix} \mathbf{a}(\omega_p)^* \\ \mathbf{a}(2\omega_p)^* \\ \mathbf{a}(3\omega_p)^* \\ . \\ . \\ . \\ \mathbf{a}(k_{max}\omega_p)^* \end{bmatrix} \tag{53}$$

and let

$$\tilde{\mathbf{a}} = \begin{bmatrix} \mathbf{a} \\ \mathbf{a}^* \end{bmatrix} \tag{54}$$

Similarly, we can define $\tilde{\mathbf{b}}$ and $\tilde{\mathbf{c}} = \tilde{\mathbf{c}}(\tilde{\mathbf{a}})$. (The functional dependence is to emphasize that the nonlinear response amplitudes for a transmission line section are a function of the incoming amplitudes for that section.) Define

$$\tilde{S} = (\oplus_{k=1}^{k_{max}} S(k\omega_p)) \oplus (\oplus_{k=1}^{k_{max}} S(k\omega_p)^*) \tag{55}$$

We define $\tilde{C}$, $\tilde{P}_i$, and $\tilde{P}_e$ to be block diagonal matrices, where each of the $2k_{max}$ blocks is a copy of C, P_i, and P_e, respectively. Then we have

$$P_i\tilde{\mathbf{a}} = \left[1 - \tilde{C}\tilde{S}\right]^{-1} \tilde{C}[\tilde{S}\tilde{P}_e\tilde{\mathbf{a}} + \tilde{\mathbf{c}}(\tilde{\mathbf{a}})] \tag{56}$$

where 1 is the $4Nk_{max} \times 4Nk_{max}$ identity matrix. Thus, we find that solving for the incoming amplitudes at each port is a root-finding exercise, where we are trying to find the root of the equation

$$L(\tilde{\mathbf{a}}) = \mathbf{0} \tag{57}$$

where L is the operator

$$L = [1 - \tilde{C}\tilde{S}]^{-1}\tilde{C}[\tilde{S}\tilde{P}_e + \tilde{\mathbf{c}}(\tilde{\mathbf{a}})] - \tilde{P}_i \tag{58}$$

To solve the equation, we apply the following iterative method:

1. Set the incoming amplitudes for the external ports, $P_e(\tilde{\mathbf{a}})$.

2. Make an initial guess for the nonlinear response amplitudes $\tilde{\mathbf{c}}(\tilde{\mathbf{a}})$. A typical guess is to set all of these amplitudes to zero.

3. Use (51) or (56) to determine the incoming port amplitudes at each harmonic.

4. For each transmission line section, compute the nonlinear response amplitudes using the perturbative solutions (32) and (33) and the power-conserving correction (43).

5. Compute $L(\tilde{\mathbf{a}})$. Compute the Newton-Raphson correction $\tilde{\delta\mathbf{a}}$ given by

$$\left(\frac{\partial L}{\partial \tilde{\mathbf{a}}}\right)\tilde{\delta\mathbf{a}} = -L(\tilde{\mathbf{a}}) \tag{59}$$

   where the derivative on the left-hand side can be computed by approximating $\tilde{\mathbf{c}}$ in equation (58) as the perturbative solution $\underline{\tilde{\mathbf{c}}}$:

$$\frac{\partial L}{\partial \tilde{\mathbf{a}}} = [1 - \tilde{C}\tilde{S}]^{-1}\tilde{C}[\tilde{S}\tilde{P}_e + \tilde{J}] - \tilde{P}_i \tag{60}$$

   where $\tilde{J}$ is a Jacobian computed in the Appendix. Eq. (59) represents a sparse linear system that can be solved for $\tilde{\delta\mathbf{a}}$.

6. Add $\tilde{\delta\mathbf{a}}$ to $\tilde{\mathbf{a}}$ to obtain a new set of incoming amplitudes at each harmonic.

7. Return to step 4. Repeat until a self-consistent solution has been reached -in other words, until the amplitudes that result in step 6 are changing negligibly from iteration to iteration. Once the solution has been reached, we have solved for the incoming amplitudes and the nonlinear response amplitudes. We can then determine the outgoing amplitudes for each harmonic, which are given by

$$\mathbf{b}(k\omega_p) = S(k\omega_p)\mathbf{a}(k\omega_p) + \mathbf{c}(k\omega_p) \tag{61}$$

Physically, this process can be thought of as follows: We solve for the pump and higher harmonic propagation in the absence of the nonlinearity (step 3). We then compute the

nonlinear response using the knowledge about pump propagation from the previous step (step 4). However, these "local" nonlinear effects affect how the pump propagates "globally" -that is, how it propagates throughout the line. Thus, we need to update our solution for the global pump and higher harmonic propagation (step 5). This, in turn, again affects the local nonlinear effects, which, in turn, affects the global pump and higher harmonic propagation. We repeat this iterative process until a self-consistent solution has been found.

Suppose we know the solution to pump propagation for some input pump power and wish to determine the solution for some higher power. Then, we need not make an initial guess of $\mathbf{0}$ for the nonlinear response amplitudes. We can set our initial guess to be those nonlinear response amplitudes which solved the system at the lower power; doing so performs the calculation in fewer iterations.

Finally, note that in numerically implementing these techniques, we describe the input pump power by a dimensionless factor:

$$a = \frac{\sqrt{P_{in}}}{2I_*^{(1)}\sqrt{Z_c^{(1)}}} \tag{62}$$

where P_{in} is the input pump power, and $I_*^{(1)}$ and $Z_c^{(1)}$ are the nonlinearity strength and characteristic impedance of the section at which the pump tone is excited. Physically, $4a^2$ can be thought of as an approximation to the maximum inductance modulation.

3. Signal Analysis in a Short Transmission Line Section

Having solved for the evolution of the pump as it travels along the loaded transmission line, we turn our attention to signal propagation, and more generally, to the sideband tones. The key assumption here is the weak-signal approximation: since the signal is weak compared to the pump, the pump amplitudes found in the previous section do not change in the presence of the signal. Similar to the manner in which we denoted pump amplitudes at each port, we write $a_1(\omega_n) = a(\omega_n; z = 0)$, $a_2(\omega_n) = b(\omega_n; z = L)$, $b_1(\omega_n) = b(\omega_n; z = 0)$, $b_2(\omega_n) = a(\omega_n; z = L)$. As before, for each transmission line section, we can write the outgoing amplitude at frequency ω_m as a sum of linear and nonlinear contributions from the incoming amplitudes:

$$\begin{bmatrix} b_1(\omega_n) \\ b_2(\omega_n) \end{bmatrix} = S(\omega_n) \begin{bmatrix} a_1(\omega_n) \\ a_2(\omega_n) \end{bmatrix} + \begin{bmatrix} c_1(\omega_n) \\ c_2(\omega_n) \end{bmatrix} \tag{63}$$

where, letting $\bar{c}$ be the section's phase velocity and $k_n = \frac{\omega_n}{\bar{c}}$ be the propagation constant,

$$S(\omega_n) = \begin{bmatrix} e^{-ik_nL} & 0 \\ 0 & e^{-ik_nL} \end{bmatrix} \tag{64}$$

Plugging the full expansion of (28) into (26) and (27), and using first-order perturbation theory,

$$\begin{aligned} \underline{c}_1(\omega_n) = \frac{ik_nL}{8I_*^2Z_c}e^{-ik_nL}\sum_{k,l,m}[&a_1(k\omega_p)a_1(l\omega_p)a_1(\omega_m)\text{sinc}(k_nL) - a_1(k\omega_p)a_1(l\omega_p)a_2(\omega_m)\text{sinc}((k_n-k_m)L) \\ &+ 2a_1(k\omega_p)a_2(l\omega_p)a_2(\omega_m)\text{sinc}(kk_pL) - 2a_2(k\omega_p)a_1(l\omega_p)a_1(\omega_m)\text{sinc}((kk_p-k_n)L) \\ &+ a_2(k\omega_p)a_2(l\omega_p)a_1(\omega_m)\text{sinc}(k_mL) - a_2(k\omega_p)a_2(l\omega_p)a_2(\omega_m)]\delta_{n,k+l+m} \end{aligned} \tag{65}$$

$$\begin{aligned} \underline{c}_2(\omega_n) = -\frac{ik_nL}{8I_*^2Z_c}e^{-ik_nL}\sum_{k,l,m}[&a_1(k\omega_p)a_1(l\omega_p)a_1(\omega_m) - a_1(k\omega_p)a_1(l\omega_p)a_2(\omega_m)\text{sinc}(k_mL) \\ &+ 2a_1(k\omega_p)a_2(l\omega_p)a_2(\omega_m)\text{sinc}((kk_p-k_n)L) - 2a_2(k\omega_p)a_1(l\omega_p)a_1(\omega_m)\text{sinc}(kk_pL) \\ &+ a_2(k\omega_p)a_2(l\omega_p)a_1(\omega_m)\text{sinc}((k_n-k_m)L) - a_2(k\omega_p)a_2(l\omega_p)a_2(\omega_m)\text{sinc}(k_nL)]\delta_{n,k+l+m} \end{aligned} \tag{66}$$

where the sums over k, l, m are from $-\infty$ to $-\infty$. As with the pump nonlinear response amplitudes, we cannot evaluate such infinite sums in a computational setting, so we truncate the sums to some sideband number s_{max}, $-s_{max} < k, l, m < s_{max}$, above which the sideband amplitudes are not significant. In deriving these expressions, we used the weak-signal approximation to ignore terms that contain fewer than two pump photons in each product of three amplitudes. Since we assume that the pump and harmonic amplitudes do not change in the presence of the signal, we can set the pump amplitudes in the above two equations to be the same as those found through the process in the previous section.

The signal cross-phase modulation effect may be seen by exciting port 1 with a pump and signal tone and not exciting port 2. Then,

$$\underline{c}_2(\omega_1 = \omega_s) = -\frac{ik_sL}{4I_*^2Z_c}e^{-ik_pL}|a_1(\omega_p)|^2a_1(\omega_s) \tag{67}$$

so

$$b_2(\omega_s) = a_1(\omega_s)e^{-ik_sL}\left(1 - \frac{ik_sL}{4I_*^2Z_c}|a_1(\omega_p)|^2\right) \approx a_1(\omega_s)\exp\left(-ik_sL - \frac{ik_sL}{4I_*^2Z_c}|a_1(\omega_p)|^2\right) \tag{68}$$

This yields a signal cross-phase modulation per unit length of

$$\Delta\phi_s = \frac{k_s|a_1(\omega_p)|^2}{4I_*^2 Z_c} = \frac{2\omega_s}{\omega_p}\Delta\phi \tag{69}$$

Similarly, we find the idler cross-phase modulation to be

$$\Delta\phi_i = \frac{k_i|a_1(\omega_p)|^2}{4I_*^2 Z_c} = \frac{2\omega_i}{\omega_p}\Delta\phi \tag{70}$$

Note that the results (69) and (70) for cross-phase modulation are the same as (17) from the coupled-mode theory.

Note also that the nonlinear response is *linear* in the sideband amplitudes. Thus, we may use matrix algebra techniques to solve for the sideband amplitudes, instead of using the complicated system in the previous section. Define a vector $\tilde{\mathbf{a}}_{sig}$ of all incoming sideband amplitudes,

$$\mathbf{a}_{sig} = \begin{bmatrix} a_1(\omega_{-s_{max}}) \\ a_2(\omega_{-s_{max}}) \\ a_1(\omega_{-s_{max}+1}) \\ a_2(\omega_{-s_{max}+1}) \\ \cdot \\ \cdot \\ \cdot \\ a_1(\omega_{-1}) \\ a_2(\omega_{-1}) \\ a_1(\omega_0) \\ a_2(\omega_0) \\ a_1(\omega_1) \\ a_2(\omega_1) \\ \cdot \\ \cdot \\ \cdot \\ a_1(\omega_{s_{max}-1}) \\ a_2(\omega_{s_{max}-1}) \\ a_1(\omega_{s_{max}}) \\ a_2(\omega_{s_{max}}) \end{bmatrix} \tag{71}$$

and similarly a vector $\underline{\mathbf{c}}_{sig}$. Then, from (65) and (66), it is clear that we can write

$$\underline{\mathbf{c}}_{sig} = S_{sig}\mathbf{a}_{sig} \tag{72}$$

where S_{sig} is a matrix of the form

$$S_{sig} = \begin{bmatrix}
S_{11}(-s_{max},-s_{max}) & S_{12}(-s_{max},-s_{max}) & S_{11}(-s_{max},-s_{max}+1) & S_{12}(-s_{max},-s_{max}+1) & \cdots & S_{12}(-s_{max},s_{max}) \\
S_{21}(-s_{max},-s_{max}) & S_{22}(-s_{max},-s_{max}) & S_{21}(-s_{max},-s_{max}+1) & S_{22}(-s_{max},-s_{max}+1) & \cdots & S_{22}(-s_{max},s_{max}) \\
S_{11}(-s_{max}+1,s_{max}) & S_{12}(-s_{max}+1,-s_{max}) & S_{11}(-s_{max}+1,-s_{max}+1) & S_{12}(-s_{max}+1,-s_{max}+1) & \cdots & S_{12}(-s_{max}+1,s_{max}) \\
S_{21}(-s_{max}+1,s_{max}) & S_{22}(-s_{max}+1,-s_{max}) & S_{21}(-s_{max}+1,-s_{max}+1) & S_{22}(-s_{max}+1,-s_{max}+1) & \cdots & S_{22}(-s_{max}+1,s_{max}) \\
S_{11}(-s_{max}+2,-s_{max}) & S_{12}(-s_{max}+2,-s_{max}) & S_{11}(-s_{max}+2,-s_{max}+1) & S_{12}(-s_{max}+2,-s_{max}+1) & \cdots & S_{12}(-s_{max}+2,s_{max}) \\
S_{21}(-s_{max}+2,-s_{max}) & S_{22}(-s_{max}+2,-s_{max}) & S_{21}(-s_{max}+2,-s_{max}+1) & S_{22}(-s_{max}+2,-s_{max}+1) & \cdots & S_{22}(-s_{max}+2,s_{max}) \\
\vdots & \vdots & \vdots & \vdots & \cdots & \vdots \\
\vdots & \vdots & \vdots & \vdots & \cdots & \vdots \\
\vdots & \vdots & \vdots & \vdots & \cdots & \vdots \\
S_{11}(s_{max},-s_{max}) & S_{12}(s_{max},-s_{max}) & S_{11}(s_{max},-s_{max}+1) & S_{12}(s_{max},-s_{max}+1) & \cdots & S_{12}(s_{max},s_{max}) \\
S_{21}(s_{max},-s_{max}) & S_{22}(s_{max},-s_{max}) & S_{21}(s_{max},-s_{max}+1) & S_{22}(s_{max},-s_{max}+1) & \cdots & S_{22}(s_{max},s_{max})
\end{bmatrix} \tag{73}$$

Using the above expressions for the nonlinear response amplitudes, the entries for this matrix are:

$$S_{11}(n,r) = \frac{ik_nL}{8I_*^2Z_c}e^{-ik_nL}\sum_{k,l}(a_1(k\omega_p)a_1(l\omega_p)\mathrm{sinc}(k_nL) - 2a_2(k\omega_p)a_1(l\omega_p)\mathrm{sinc}((kk_p - k_n)L) + a_2(k\omega_p)a_2(l\omega_p)\mathrm{sinc}(k_rL))\delta_{n,k+l+r} \tag{74}$$

$$S_{12}(n,r) = -\frac{ik_nL}{8I_*^2Z_c}e^{-ik_nL}\sum_{k,l}(a_1(k\omega_p)a_1(l\omega_p)\mathrm{sinc}((k_n - k_r)L) - 2a_1(k\omega_p)a_2(l\omega_p)\mathrm{sinc}(kk_pL) + a_2(k\omega_p)a_2(l\omega_p))\delta_{n,k+l+r} \tag{75}$$

$$S_{21}(n,r) = -\frac{ik_nL}{8I_*^2Z_c}e^{-ik_nL}\sum_{k,l}(a_1(k\omega_p)a_1(l\omega_p) - 2a_2(k\omega_p)a_1(l\omega_p)\mathrm{sinc}(kk_pL) + a_2(k\omega_p)a_2(l\omega_p)\mathrm{sinc}((k_n - k_r)L))\delta_{n,k+l+r} \tag{76}$$

$$S_{22}(n,r) = \frac{ik_nL}{8I_*^2Z_c}e^{-ik_nL}\sum_{k,l}(a_1(k\omega_p)a_1(l\omega_p)\mathrm{sinc}(k_rL) - 2a_1(k\omega_p)a_2(l\omega_p)\mathrm{sinc}((kk_p - k_n)L)$$
$$+ a_2(k\omega_p)a_2(l\omega_p)\mathrm{sinc}(k_nL))\delta_{n,k+l+r} \tag{77}$$

4. Signal Analysis in a Cascade of Short Transmission Lines

Now we analyze signal propagation in the context of the full cascade. For each sideband frequency ω_m, define a vector of the incoming amplitudes for all sections:

$$\mathbf{a}(\omega) = \begin{bmatrix} a_1^{(1)}(\omega_m) \\ a_2^{(1)}(\omega_m) \\ a_1^{(2)}(\omega_m) \\ a_2^{(2)}(\omega_m) \\ . \\ . \\ . \\ a_1^{(N)}(\omega_m) \\ a_2^{(N)}(\omega_m) \end{bmatrix} \tag{78}$$

As in the harmonic balance treatment for the pump, the superscript represents the section index. We define similar vectors $\mathbf{b}(\omega_m)$ and $\mathbf{c}(\omega_m)$ for the outgoing and nonlinear response amplitudes. Note that every other pair of entries in the nonlinear response vector will be zero because impedance-conversion circuits are linear. For each sideband frequency, we define the $2N \times 2N$ scattering matrix

$$S(\omega_m) = \oplus_{s=1}^{N} S^{(s)}(\omega_m) \tag{79}$$

where $S^{(s)}(\omega_m)$ is the linear scattering matrix from equation (64) representing the linear propagation phase shifts for the sth section.

Following Eq. (51), the sideband amplitudes at the internal ports are given by

$$P_i\mathbf{a}(\omega_m) = [1 - CS(\omega_m)]^{-1}C[S(\omega)P_e\mathbf{a}(\omega_m) + \underline{\mathbf{c}}(\omega_m)] \tag{80}$$

where we have substituted the perturbative solution $\underline{\mathbf{c}}(\omega_m)$ for the actual nonlinear response amplitudes $\mathbf{c}(\omega_m)$. Using the concatenation scheme of (56)-(54), we arrive at

$$\tilde{P}_i\tilde{\mathbf{a}}_s = \left[1 - \tilde{C}\tilde{S}\right]^{-1}\tilde{C}[\tilde{S}\tilde{P}_e\tilde{\mathbf{a}}_s + \underline{\tilde{\mathbf{c}}}_s] \tag{81}$$

where

$$\tilde{S} = \oplus_{k=-s_{max}}^{s_{max}} S(\omega_k) \tag{82}$$

$$\tilde{\mathbf{a}}_s = \begin{bmatrix} \mathbf{a}(\omega_{-s_{max}}) \\ \mathbf{a}(\omega_{-s_{max}+1}) \\ \cdot \\ \cdot \\ \cdot \\ \mathbf{a}(\omega_{s_{max}}) \end{bmatrix} \tag{83}$$

and similarly for $\underline{\tilde{\mathbf{c}}}_s$. From (72), it is clear that we can write

$$\underline{\tilde{\mathbf{c}}}_s = \tilde{S}_{sig}\tilde{\mathbf{a}}_s \tag{84}$$

where $\tilde{S}_{sig}$ is constructed from the nonlinear scattering matrices for each section. Plugging this into Eq. (81),

$$\tilde{P}_i\tilde{\mathbf{a}}_s = \left[1 - \tilde{C}\tilde{S}\right]^{-1} \tilde{C}[\tilde{S}\tilde{P}_e\tilde{\mathbf{a}}_s + \tilde{S}_{sig}\tilde{\mathbf{a}}_s] \tag{85}$$

Rearranging,

$$\tilde{P}_i\tilde{\mathbf{a}}_s = [1 - \tilde{C}(\tilde{S} + \tilde{S}_{sig})]^{-1}\tilde{C}(\tilde{S} + \tilde{S}_{sig})\tilde{P}_e\tilde{\mathbf{a}}_s \tag{86}$$

Equation (86) gives the incoming amplitudes at the internal ports in terms of the incoming amplitudes at the external ports, the latter of which is a known parameter because it represents the sideband amplitudes which are excited at the ends of the transmission line cascade. Once the incoming amplitudes at all ports are found, the outgoing amplitudes at each sideband frequency may be found through

$$\tilde{\mathbf{b}}_s = \tilde{S}\tilde{\mathbf{a}}_s + \underline{\tilde{\mathbf{c}}}_s = (\tilde{S} + \tilde{S}_{sig})\tilde{\mathbf{a}}_s \tag{87}$$

where $\tilde{\mathbf{b}}_s$ is defined similarly to $\tilde{\mathbf{a}}_s$.

To summarize, the harmonic balance model operates as follows: First, using an iterative Newton-Raphson method, we solve for the pump and higher harmonic propagation. Then, using the weak-signal approximation and linear algebra techniques, we solve for the signal and sideband propagation.

III. GAIN AND POWER-DEPENDENT PHASE PROCESSES OBSERVED IN THE DTWKI AMPLIFIER

In this chapter, we discuss experimental results concerning gain and power-dependent phase processes observed in the DTWKI amplifier and progress toward achieving high gain-bandwidth. A typical experimental setup is shown in Fig. 7 from [1].

A. Device I

The first sample studied was that shown in Fig. 2. For several different pump powers, we measured the forward signal transmission in a wide range around the optimal pump frequency of 11.56 GHz. (By optimal, we mean that this pump frequency gave the highest gain.) The gain of the signal can be computed by dividing the measured transmission amplitude when the pump is on by the measured transmission amplitude when the pump is off. The unnormalized pump-off transmission (the transmission in the absence of nonlinearity) for this device is shown in Fig. 8. The transmission dips/stopbands shown are centered at 5.90 GHz, 11.83 GHz, 17.70 GHz. Note that we opted to use the second dispersion feature, instead of the first, as to increase the dispersion at the pump. (There is a transmission dip near 35 GHz that blocks the third pump harmonic.)

To elucidate the physical mechanisms behind DTWKI operation, the results were compared to the harmonic balance model described in Sec. 2B. For these simulations, we considered the first three harmonics and the first seven sidebands, $k_{max} = s_{max} = 3$. Note that these simulations do not take into account the port impedance, so the effects of impedance mismatch between the transmission line and the ports- and in particular, reflections- are not modeled.

In comparing to the model, we first calculate, for each piece of thin-film CPW in the six-block periodic structure, the characteristic impedance and phase velocity. These parameters are then adjusted to match the width and center frequency of the dispersion feature near the pump in the pump-off transmission.

Additionally, to convert the physical power scale to the dimensionless power scale used in simulation, a conversion factor is computed; this is done by finding the pump power on the dimensionless scale such that, for signal frequencies near the pump, the simulated amplifier

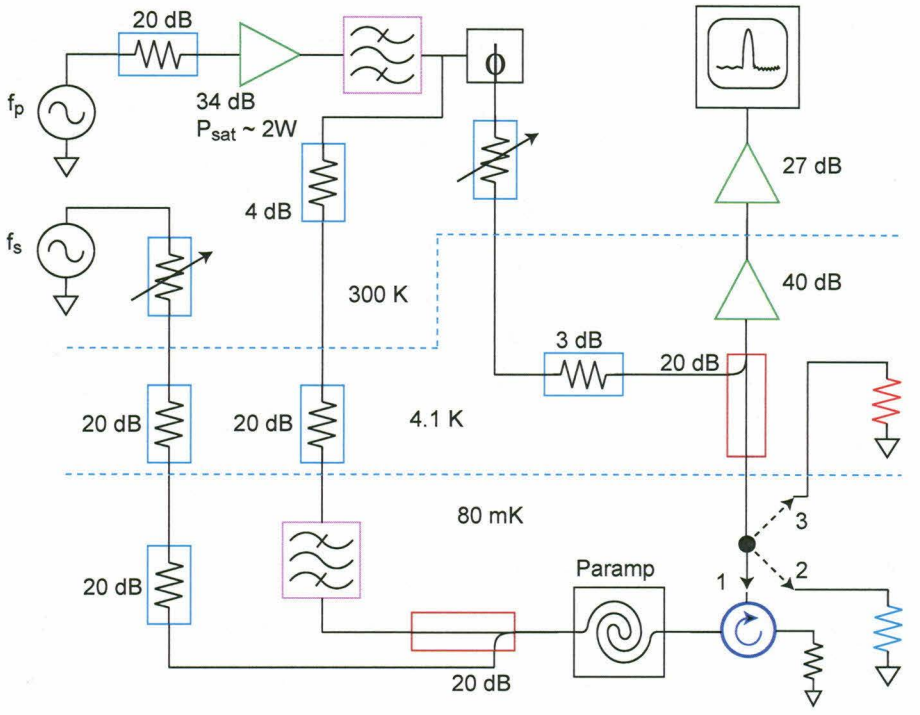

FIG. 7. An experimental setup for testing DTWKI amplifiers. The pump is produced by a low noise synthesizer, amplified to an appropriate level, and then filtered by a commercial combine filter. After passing through a splitter, the pump is attenuated at 4 K. This tone is then filtered through a second commercial combine filter, which provides more than 70 dB attenuation of noise on the pump line at the signal frequencies of interest and prevents synthesizer phase noise from appearing as noise at the signal frequency. The other output of the splitter is phase and amplitude adjusted to cancel the pump tone that passes through the paramp. Without cancellation, the pump power would saturate the 4 K HEMT amplifier. The signal tone is produced by another low-noise synthesizer or a vector network analyzer. After passing through several attenuators at both room temperature and the 4 K stage, the signal is coupled to the paramp input by a 20 dB directional coupler at the base temperature of the dilution refrigerator. A cryogenic isolator placed after the paramp is used to absorb noise radiated from the HEMT towards the paramp in the post-amplification stage. A cryogenic switch allows the HEMT to be connected to 50 Ω loads at the base temperature and 4K stages, which enables the noise measurement process. After further room temperature amplification, the signal is measured using the network analyzer. Note that losses from coaxial cables are not displayed.

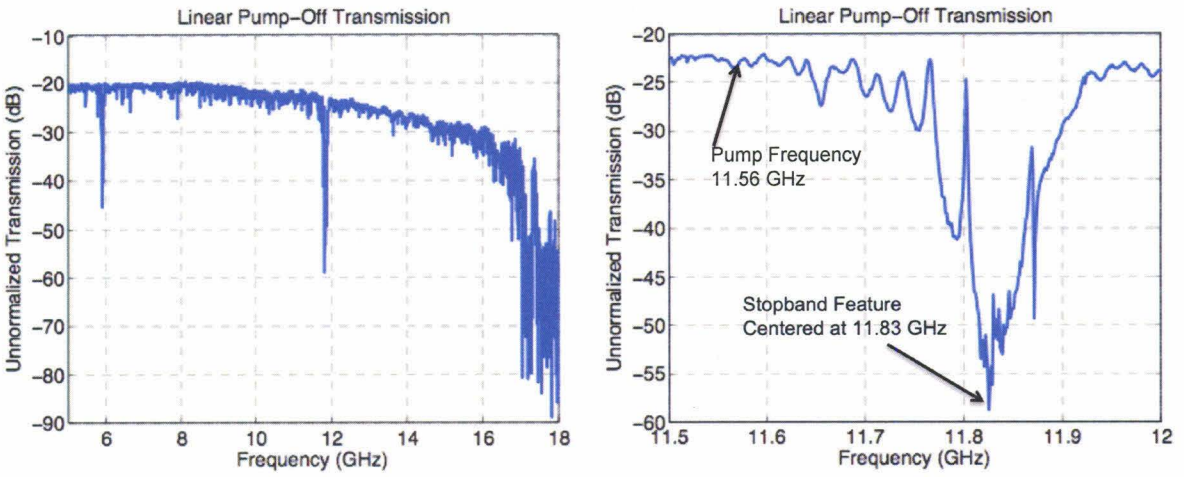

FIG. 8. The measured pump-off transmission for the DTWKI device shown in Fig. 2. **Left**: The pump-off transmission in the frequency range 5-18 GHz. Note the stopband features centered at 5.90 GHz, 11.83 GHz, 17.70 GHz. The decrease in unnormalized transmission at higher frequencies is primarily due to losses in the coaxial lines. **Right**: A close-up of the pump-off transmission in the frequency range 11.5-12 GHz, with the pump frequency and the stopband feature, which provides the pump dispersion, labeled.

gain at that power matches the experimental amplifier gain at the highest applied physical power. The power conversion process is illustrated in Fig. 9. The amplifier gain (blue curve) near the pump at the highest applied pump power, -7.61 dBm (0.173 mW), was matched by setting the pump power in simulation to $a_{max} = 0.059$ (green curve). (Above -7.61 dBm, the critical power is exceeded and the superconducting thin films switch to the normal state, at which point the pump power is dissipated and no gain is observed.) Dividing a_{max}^2 by the highest applied power in Watts gives the multiplicative factor for converting physical powers. In this case, the conversion factor was $0.059^2/0.000173$=20.12. Given a physical power in Watts, multiplying the power by the conversion factor gives the corresponding a^2-value. Taking the square root then gives the desired a-value.

Analyzing the experimental gain curve in the top panel of Fig. 9, we see that the amplifier achieves significant gain at $a_{max} = 0.059$ (-7.61 dBm) in the frequency range 8-14 GHz. However, there is a fine-scale variation of the gain that varies periodically with the signal frequency. This variation increases with pump power, and diverges around the critical power, at which nonlinear dissipation arises. As a result, though the average gain is approximately

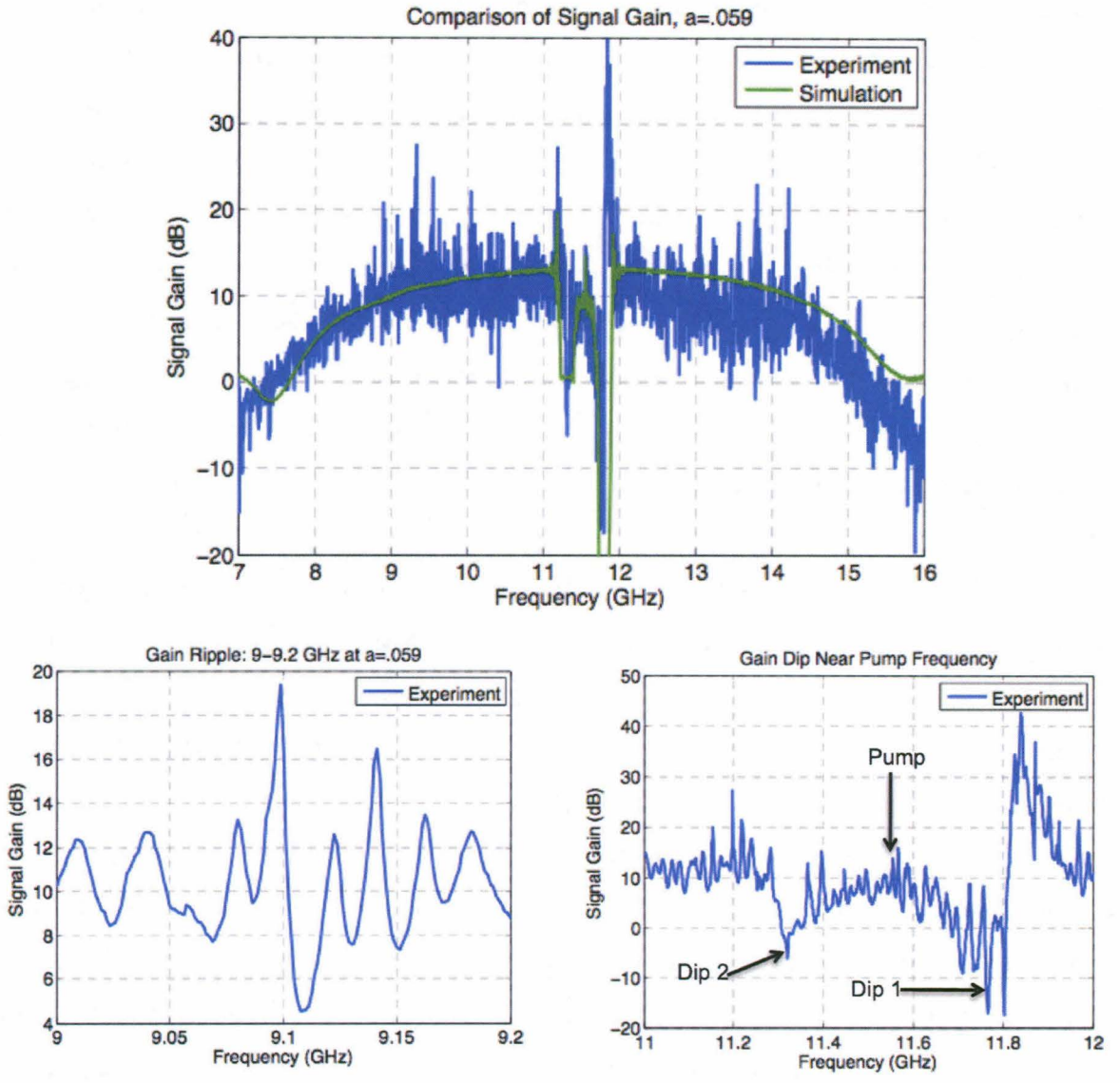

FIG. 9. **Top**: A comparison between experiment and simulation of the gain profile at power $a_{max} = 0.059$. The experimental curve is shown in blue, while the simulated curve is shown in green. The peak in the experimental gain near 12 GHz is an artifact of the analysis procedure. The transmission dip at that frequency shifts to lower frequency when the pump is applied, producing a peak in the ratio of the pump on to pump off transmission. **Bottom Left**: A sample of the gain ripple at power $a_{max} = .059$ between 9 and 9.2 GHz. On average, the ripple has a height of 5 dB, with the ripple height reaching more than 12 dB near 9.1 GHz. **Bottom Right**: The two gain dips observed near the pump frequency. Dip 1 is located near 11.8 GHz, whereas Dip 2 is near 11.3 GHz.

10 dB, several peaks above 20 dB are observed. The frequency spacing of the peaks in the gain ripples (bottom left panel of Fig. 9), approximately 25 MHz, corresponds to the electrical length of the transmission line, indicating that the gain ripple is due to standing waves created at the ends of the line. The origin of these standing waves is two-fold. First, because of the dispersion, the impedance at the pump frequency is significantly different from the characteristic impedance. Indeed, a Bloch-type solution to the six-cell periodic structure reveals a pump impedance of nearly 220 Ω. Such an impedance mismatch between the taper (which has impedance of 300 Ω at the ends of the amplifier) and the amplifier creates reflections and consequently, standing waves. Second, the impedance of the tapers at the input and output ports of the amplifier may differ from 50 Ω, which is the impedance of the external circuit.

The limits which impedance mismatch place on gain can be understood quantitatively. Consider the transmission line cascade drawn in Fig. 6. For a signal wave propagating from external port 2 to external port 1, let Γ_1 represent the fraction of power that is reflected at external port 1. For a wave propagating from external port 1 to external port 2, let Γ_2 represent the fraction of power that is reflected at external port 2. For simplicity, let $\Gamma = \Gamma_1 = \Gamma_2$. Let G_f represent the forward gain -the gain the signal acquires in traveling from port 1 to port 2- and let G_b represent the backward gain -the gain the signal acquires in traveling from port 2 to port 1. Recent DTWKI experiments have demonstrated that the backward gain is, to excellent approximation, $G_b = 1$. Consider a signal wave with input power amplitude P_s at external port 1. It travels to external port 2, where it is reflected, creating a backward-traveling wave with power amplitude $\Gamma G_f P_s$. This wave is reflected at external port 1, creating a forward-traveling wave with power amplitude $\Gamma^2 G_f P_s$. If

$$\Gamma^2 G_f > 1 \tag{88}$$

then the new forward-traveling wave has a greater amplitude than the input signal. After many oscillations, the signal amplitude will exceed the critical power; when this occurs, the DTWKI will switch to a resistive state, and the power in the line will be dissipated. We term this phenomenon *self-oscillation.* The greater the impedance mismatch, the greater the reflection coefficient Γ, and the lower the forward gain G_f at which the critical power is exceeded.

Note that there are two dips in the signal gain near the pump frequency, as shown in

the bottom right panel of Fig. 9. The dip labeled "Dip 1" in the figure, occurring near 11.8 GHz, occurs because these signal frequencies fall in the stopband in the right panel of Fig. 8. Any pump to signal power conversion is overcome by the attenuation in the forward-traveling signal power. The dip labeled "Dip 2" in the figure, occurring near 11.3 GHz, occurs because the idler falls in the stopband; since the amount of signal gain depends critically on the coherent interaction of pump, signal, and idler, and since the idler is attenuated as it travels through the line, no signal gain is observed. As demonstrated in Fig. 4, the coupled-mode equations do not predict these gain dips; this is due to the fact that in assuming the transmission line possesses intrinsic dispersion-as opposed to dispersion caused by periodic loadings-, we ignore transmission stopbands.

Though we chose the power conversion factor to match the experimental and simulated gain near the pump, the gain is also reasonably matched at signal frequencies far from the pump. This indicates that the added dispersion at the pump is providing the gain-bandwidth enhancement predicted by the harmonic balance model with $s_{max} = 3$.

An interesting feature arises when we examine the gain profile for lower powers, such as $a = 0.0399$ (-11 dBm). The gain profile is shown in the top plot of Fig. 10; as in the gain profile at a_{max}, the simulated profile at $s_{max} = 3$ (green curve) and the experimental profile (blue curve) are reasonably matched over a large range of frequencies. For signal frequencies near 7 GHz, the amplifier is observed as operating in a deamplification mode with >15 dB deamplification; that is, the output signal power is less than 1/30-th of the input signal power. From equations (14) and (15), it is clear that the coupled-mode equations, considering only pump, signal, and idler, do not predict deamplification when the linear phase mismatch $\Delta\beta$ is less than zero. Accordingly, the deamplification mode is not predicted when we run the gain simulation with $s_{max} = 1$, shown in red in Fig. 10. However, the $s_{max} = 3$ model predicts that deamplification will occur (albeit at a frequency 200-300 MHz greater than what is observed). How do we resolve this discrepancy?

The resolution to this discrepancy lies in understanding the conversion of the signal ω_s into the third harmonic sideband frequency $\omega_3 = 2\omega_p + \omega_s$. The principal process for the production of ω_3 photons is the combination of one signal photon and two pump photons. As in the conversion of two pump photons to a signal and idler photon, the rate of production is dictated by the degree of phase mismatch between the pump, signal, and ω_3 tones. In designing early DTWKI devices, (before the harmonic balance model had been fully devel-

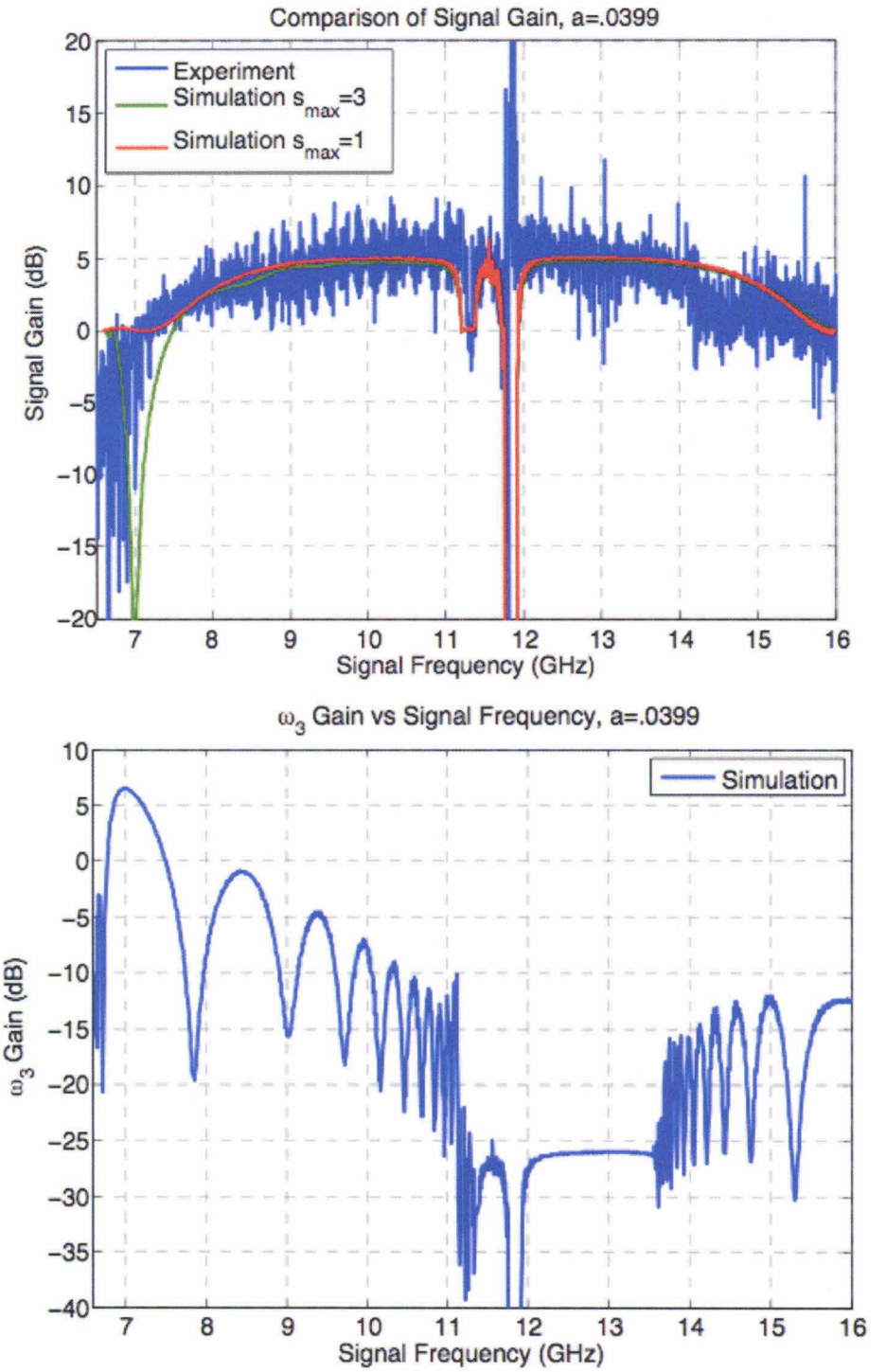

FIG. 10. **Top**: Gain profile at $a = 0.0399$, as measured in experiment (blue curve), computed in simulation at $s_{max} = 3$ (green curve), and computed in simulation at $s_{max} = 1$ (red curve). **Bottom**: Simulated gain of the ω_3 tone as a function of signal frequency.

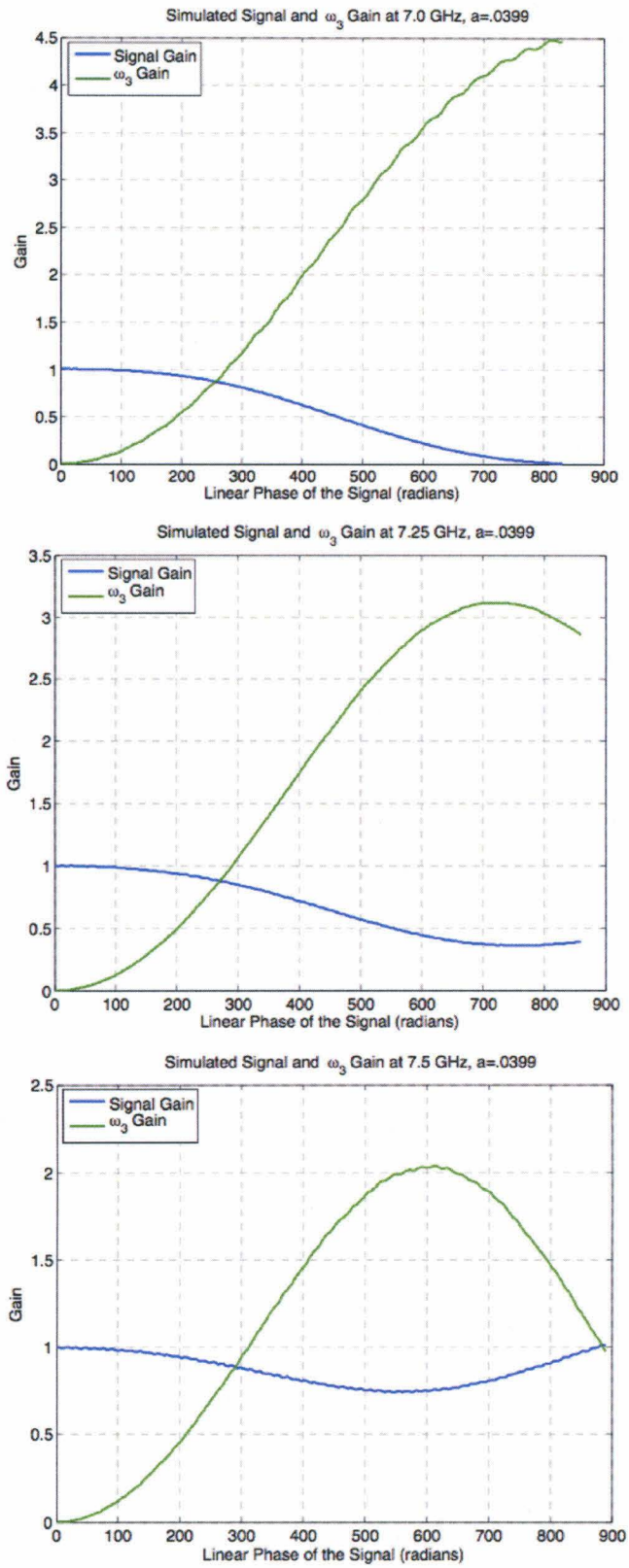

FIG. 11. The simulated signal and ω_3 gain vs linear phase of the signal for signal frequencies 7.0 GHz, 7.25 GHz, and 7.5 GHz. Note that the gain is not in logarithmic (dB) units.

oped) it had been assumed that for most signal frequencies, the third harmonic sideband frequency should fall in the wide stopband at the third harmonic and that for signal frequencies for which this does not occur, there is significant phase mismatch generated by the added dispersion outside of the stopband; in either case, the generation of the ω_3 tone should be suppressed to negligible levels. Plotted in the bottom panel of Fig. 10 is the simulated gain in the ω_3 tone, $G_3 = \frac{\text{Output Power at Frequency } \omega_3}{\text{Input Signal Power}}$, versus the signal frequency. Note that at some frequencies near 7 GHz -frequencies for which the lower third harmonic sideband does not fall in the stopband- G_3 is more than 6 dB. The power in the ω_3 output is greater than that in the signal output, and the ω_3 tone cannot be ignored.

To better understand why the ω_3 tone is a significant factor for the production of signal gain, we plot in Fig. 11 the simulated signal and ω_3 gain versus the linear phase of the signal for signal frequencies 7.0 GHz, 7.25 GHz, and 7.5 GHz. The linear phase of the signal is the phase the signal would have at some point on the line in the absence of nonlinearity; it is linearly proportional to the distance along the line.

The evolution of the signal and ω_3 amplitude can be semi-quantitatively described by extending the coupled-mode treatment of Section 2A to include the ω_3 tone, whose slowly-varying complex amplitude we represent by A_3 and whose wavenumber we represent by k_3. We write, for each tone,

$$A_\alpha(z) = |A_a(z)|\exp(i\theta_\alpha(z)) \tag{89}$$

We then find that

$$\frac{dP_s}{dz} \propto \sqrt{P_s(z)}\sqrt{P_i(z)}\cos(\kappa_1(z)) - \sqrt{P_s(z)}\sqrt{P_3(z)}\cos(\kappa_3(z)) \tag{90}$$

$$\frac{dP_3}{dz} \propto \sqrt{P_s(z)}\sqrt{P_3(z)}\cos(\kappa_3(z)) \tag{91}$$

where the constant of proportionality is positive and P_s and P_3 are the power amplitudes for the signal and ω_3 tones, respectively.

$$\begin{aligned}
\kappa_1(z) &= \Delta\beta_1 + \theta_s(z) + \theta_i(z) - 2\theta_p(z) \\
\kappa_3(z) &= \Delta\beta_3 + \theta_3(z) - \theta_s(z) - 2\theta_p(z) \\
\Delta\beta_1 &= k_s + k_i - 2k_p \\
\Delta\beta_3 &= k_3 - k_s - 2k_p
\end{aligned} \tag{92}$$

The first term on the right-hand side in (90) relates to the mixing of two pump photons, a signal photon, and an idler photon. If the term is positive, the two pump photons are being

converted to a signal photon and an idler photon; if it is negative, the signal photon and idler photon are being converted to two pump photons. The second term in (91) relates to the mixing of two pump photons, a signal photon, and an ω_3 photon. If the term is positive (with the inclusion of the minus sign), an ω_3 photon is being converted to two pump photons and a signal photon. If the term is negative, two pump photons and a signal photon are being converted to an ω_3 photon. Note that the term on the right-hand side of (91) carries the opposite sign of the second term on the right-hand side of (90). This represents that as the ω_3 power decreases, the signal power increases. $\kappa_1(z)$ and $\kappa_3(z)$ are simply a measure of the phase mismatch between tones. Considerations of translational symmetry, owing to the periodic structure of the DTWKI, allow us to approximate $\kappa_1(z)$ and $\kappa_3(z)$ as linear functions

$$\begin{aligned} \kappa_1(z) &\approx \gamma_1^0(\omega_s) + \gamma_1^1(\omega_s)z \\ \kappa_3(z) &\approx \gamma_3^0(\omega_s) + \gamma_3^1(\omega_s)z \end{aligned} \tag{93}$$

for some frequency-dependent coefficients $\gamma_1^0(\omega_s)$, $\gamma_1^1(\omega_s)$, $\gamma_3^0(\omega_s)$, and $\gamma_3^1(\omega_s)$.

All three plots in Fig. 11 illustrate a sinusoidal variation of the signal and ω_3 tone. Such behavior is predicted by the cosine term with the linear-in-z argument (calculated in (93)) in equations (90) and (91). In the top panel, corresponding to signal frequency 7 GHz, the power in the ω_3 tone increases at the expense of the signal power throughout the transmission line; the power in the ω_3 tone seems to level off at the end of the line. This process can be seen using (90) and (91) by varying $\kappa_3(z)$ from 0 to $\frac{\pi}{2}$; in such a situation, the term on the right-hand side of (91) is always positive, so the ω_3 amplitude increases. As $\kappa_3(z)$ approaches $\frac{\pi}{2}$, the derivative in (91) approaches zero and the growth begins to level off, as illustrated in the figure. An important question to ask is why the power in the lower sideband of the third harmonic can exceed the input signal power. If all the power in the input is converted into higher sideband power, from where does the extra power in the sideband originate? The answer to this question lies in the first term of equation (90). While the third harmonic sideband is taking away power from the input signal, additional signal power is generated by pump-to-signal conversion. The higher harmonic sideband extracts this signal power as well, causing the signal amplitude to always decrease and increasing the higher harmonic sideband power beyond the input signal power.

In the middle panel, corresponding to the signal frequency 7.25 GHz, the power in the ω_3

tone increases at the expense of the signal power until a linear signal phase of approximately 700 radians. Beyond 700 radians, the process is reversed: the power in the higher sideband tone decreases, whereas the signal power increases. This process is understood by varying $\kappa_3(z)$ from 0 to a value between $\frac{\pi}{2}$ and $\frac{3\pi}{2}$. From (91), between 0 and $\frac{\pi}{2}$, the derivative is positive and the ω_3 tone grows. When $\kappa_3(z)$ reaches $\frac{\pi}{2}$, corresponding to the linear signal phase reaching 700 radians, the derivative of (91) reaches zero, and the ω_3 tone is at maximum amplitude. Now, as $\kappa_3(z)$ grows beyond $\frac{\pi}{2}$, the derivative of (91) is negative, meaning that the ω_3 photons begin to convert back into signal photons, as illustrated in the figure.

The bottom panel, corresponding to the signal frequency 7.5 GHz, shows the same effect as the middle panel, with the exception that the amount of distance over which the signal amplitude increases is greater in the former plot. In other words, letting L be the length of the transmission line, $\kappa_3(z = L)$ is greater in the first situation than in the second, but in both situations, the value is less than $\frac{3\pi}{2}$.

In summary, in some instances, we are not able to ignore the ω_3 tone because the tone can inhibit signal gain.

In addition to analyzing the signal gain as a function of signal frequency, we can analyze the signal gain as a function of pump power. For the remainder of this section, all simulations are performed with $k_{max} = s_{max} = 3$. The comparison of simulation and experiment is shown in Fig. 12. The signal frequency is 9.5 GHz; to account for the gain ripple, we average the signal gain data points in the 200 MHz band centered around 9.5 GHz. The plot shows a reasonable match between simulation and experiment, with the only exception being gain at high pump powers. The decrease in gain above $a = 0.05$ (1% maximum inductance modulation) is likely due to dissipation effects related to quasiparticle generation. The simulation does not take into account loss mechanisms in superconductors- hence, the difference between the data and model output. Indeed, as described in Section 2B, we assume that power is conserved as waves travel through the transmission line.

Our analysis of the data reveals that the harmonic balance model predicts with significant accuracy the behavior of the signal amplitude as a function of pump power and signal frequency. A natural question to ask is whether the model also accurately predicts the signal phase. From the forward transmission data, we can infer the power-dependent phase contribution to the total signal phase as a function of signal frequency and pump power.

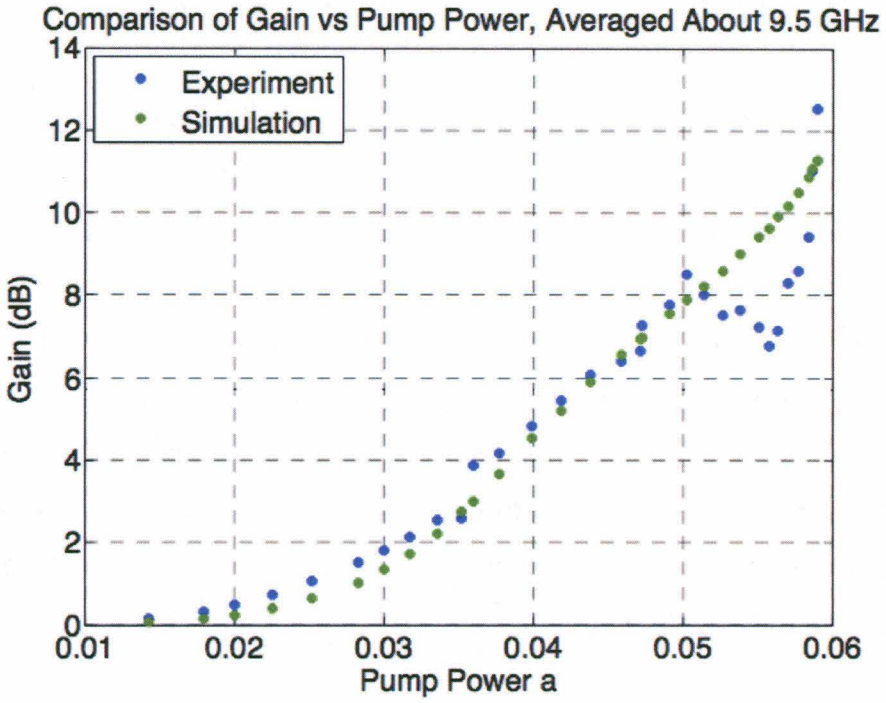

FIG. 12. Signal gain at 9.5 GHz as a function of pump power, as measured in experiment (blue curve) and computed in simulation (green curve). To account for the gain ripple, we average the gain values in the 200 MHz band around the signal frequency.

This is done by measuring the phase of the transmitted signal when the pump is on and measuring the phase of the transmission when the pump is off. Subtracting the second value from the first yields the power-dependent phase. From equation (14), we deduce that the power-dependent phase is the sum of the signal cross-phase modulation and terms arising from phase mismatch (i.e. the terms which contain κ).

The top panel of Fig. 13 illustrates reasonable agreement between the power-dependent phase measured at the highest pump power $a_{max} = 0.059$ and that computed in simulation for signal frequencies 7-15 GHz. Note that the phase demonstrates a fine-scale variation with the frequency spacing of ripple peaks being approximately 25 MHz; this is not surprising as the gain profile shows the same behavior. It is almost certain that the phase ripple is due to the same impedance mismatch issues. The discrepancy between simulation and experiment near 15 GHz is likely due to the differing depths of the strong stopband feature located at 17.7 GHz (see Fig. 8). In simulation, the transmission stopband has a depth greater than 1000 dB. (Because of numerical precision issues, a depth of 1000 dB means

that the transmitted amplitude is essentially zero.) Such a deep stopband is not possible in experiment, with the deepest observed stopbands having a depth of 60 dB; indeed, looking at Fig. 8, the stopband at 17.7 GHz, which is the largest of the three, has a measured depth of approximately 50 dB. A deeper stopband feature means greater dispersion far from the stopband, which in turn, translates to a discrepancy between model and experiment in the wavenumber k_s. This results in a discrepancy in the linear phase mismatch, which from (14), produces a discrepancy in the power-dependent contribution to the phase.

Interestingly, if the signal phase given by the coupled-mode equations is approximately correct (which we believe it is), the data displayed in Fig. 13 allows us to deduce whether phase-matching -and consequently, maximum gain- is achieved. From equation (14), if the power-dependent phase approaches zero as the signal frequency approaches zero, then the line is phase-matched. In Fig. 13, the power-dependent phase in the limit of zero frequency is approximately -4 radians. Thus, the line is not phase-matched. There are several possibilities for why the optimal pump frequency does not give phase-matched gain. For example, the pump that is theoretically predicted to give phase-matched gain (i.e. the theoretically-predicted optimal pump frequency) could be closer to the stopband than the experimentally-observed optimal pump frequency. In this case, the electrical impedance at the theoretically-predicted pump is greater than that at the experimentally-observed pump, which, in turn, implies a greater impedance mismatch between the taper and the DTWKI device. The gain at which self-oscillation leads to power dissipation is then lower, which compensates for any extra gain performance that would result from phase-matching.

The bottom panel of Fig. 13 demonstrates reasonable agreement between measurements and model output of power-dependent phase as the pump power is varied. The signal frequency is fixed at 9.5 GHz. To account for the phase ripple, we use the same technique that we used to account for the gain ripple. That is, we average the phase data points in the 200 MHz band centered around 9.5 GHz. The difference between simulated power-dependent phase and experimental power-dependent phase is slightly larger for pump powers higher than $a = 0.05$. While the reason for this is unknown, the gain discrepancy is also larger for pump powers higher than $a = 0.05$; since the gain discrepancy is most likely caused by dissipation in the superconducting thin films, it is possible that the phase discrepancy is also due to dissipation.

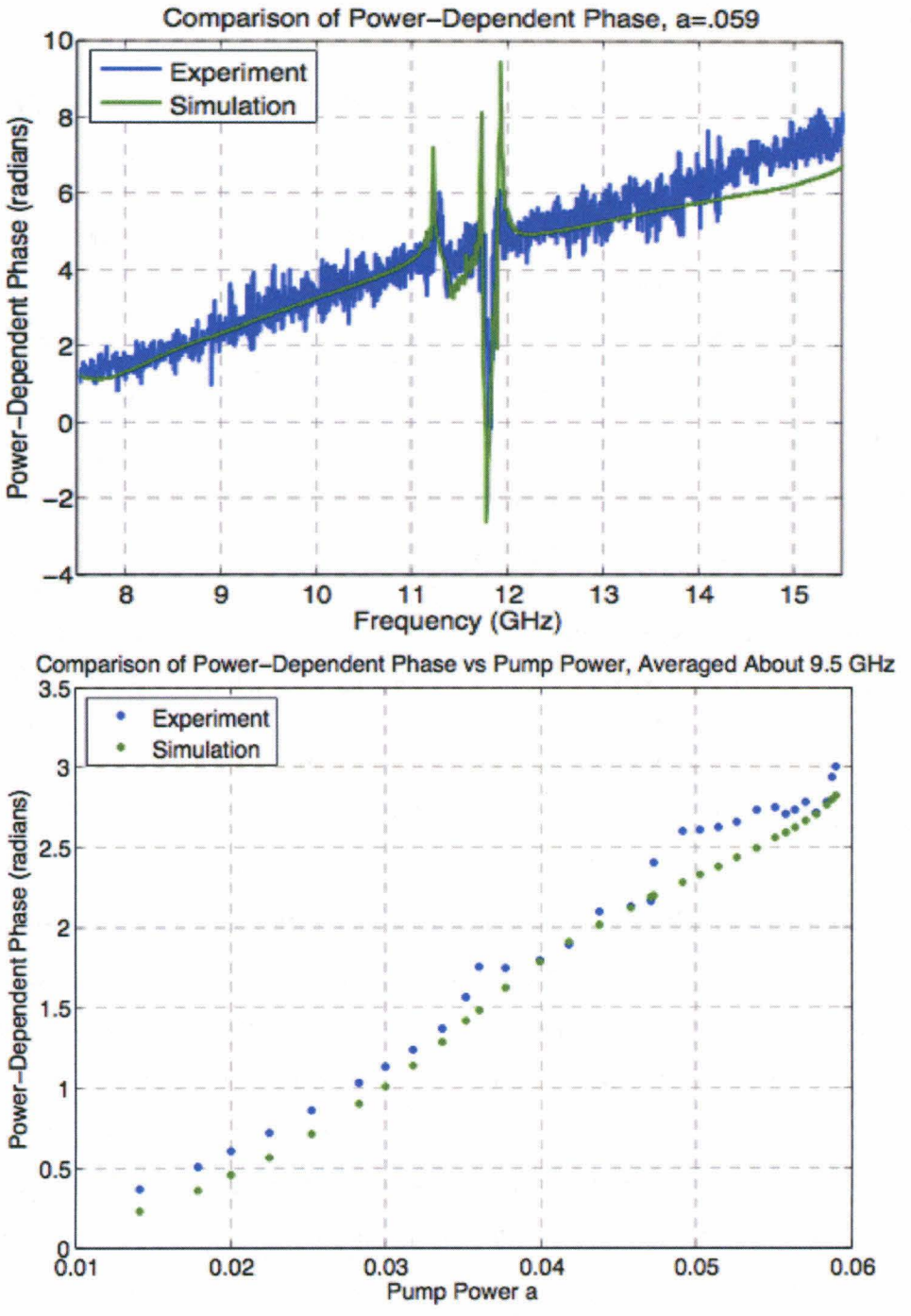

FIG. 13. **Top**: Power-dependent phase at $a_{max} = 0.059$ as a function of signal frequency, as measured in experiment (blue curve) and computed in simulation (green curve). **Bottom**: Power-dependent phase at 9.5 GHz as a function of pump power. To account for the phase ripple, we average the phase values in the 200 MHz band centered at the signal frequency.

B. Device II

From the previous section, we observed two effects that can limit gain-bandwidth performance:

1. The impedance mismatch, which is likely caused by the dispersion at the pump and a mismatch between the taper impedance and the characteristic impedance of the amplification section, can result in inconsistent gain performance over a wide range of frequencies. For example, in Device I, large gain ripples were observed in the 8-14 GHz range. The impedance mismatch also likely limits the gain due to self-oscillation. Additionally, the impedance mismatch may prevent the amplifier from achieving broadband phase-matched gain.

2. Significant power transfer from the signal to the third harmonic sideband at frequency $\omega_3 = 2\omega_p + \omega_s$ can reduce the signal gain and bandwidth.

We chose to attack the first issue. Our proposed solution to the problem was as follows:

Suppose that instead of choosing every third loading in the DTWKI to be one-half of the length of the other two loadings, we slowly "phase in" the reduced-length loading. That is, at one end of the line, we allow the three loadings in the six-block periodic structure to all be the same length. Then, as we progress along the line, we gradually reduce the length of every third loading until the third loading is one-half of the length of the other two loadings in the six-block structure. We maintain the one-half-length third loading for a certain length of line; as we approach the other end of the line, we gradually increase the length of the third loading until, at the very end of the line, it equals the length of the first two loadings.

Because of the phased-in loading, while significant pump dispersion exists in the center of the line, there is no dispersion at the ends of the line. Since there is no dispersion, the electrical impedance for the pump should, to excellent approximation, be equal to the characteristic impedance of the transmission line. The mismatch between the taper and the filter section should therefore be smaller. Since we vary the amount of dispersion at the pump, the phase-matching condition (23) cannot be met at all points along the line, and therefore, inefficiency in signal generation is introduced. The gain inefficiency should however be balanced–over even overcome– by the higher self-oscillation threshold: since the impedance mismatch is lower, the gain at which self-oscillation occurs is higher.

We fabricated and measured a device with the phased-in loading feature. The distance between loadings is 626 μm. The first three loadings at one end of the line have lengths 50, 50, and 50 μm. Over the first 0.2 meters, the third 50 μm loading is slowly reduced in length to 25 μm. The 25 μm length is maintained over the next 0.25 meters. Over the last 0.2 meters, the loading is gradually increased in length from 25 μm back to 50 μm.

The pump-off transmission for this device is shown in Fig. 14. In the range shown, there is one stopband, which is centered at 8.86 GHz. The measured optimal pump frequency is 8.694 GHz. Instead of using the second dispersion feature, as we did in Device I, we used the first dispersion feature.

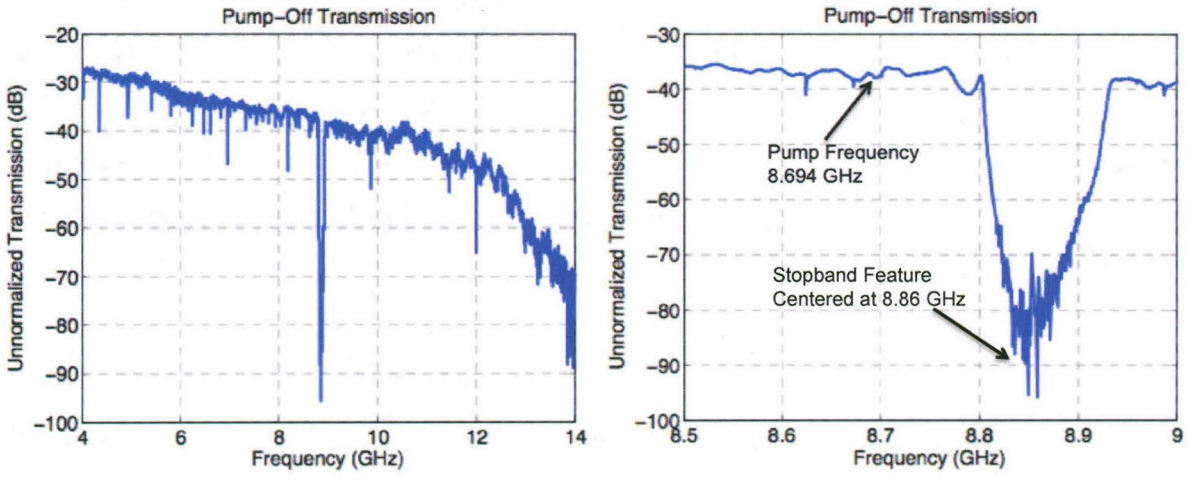

FIG. 14. The measured pump-off transmission for the DTWKI Device II, including some loss from external components. **Left**: The pump-off transmission in the frequency range 4-14 GHz. There is one stopband feature, which is centered at 8.86 GHz. As in Device I, the decrease in unnormalized transmission at higher frequencies is likely due to coaxial losses. **Right**: A magnified view of the pump-off transmission in the frequency range 8.5-9 GHz, with the pump frequency and the stopband feature labeled.

Now that the pump wavenumber is position-dependent, the analytical solutions to coupled-mode equations derived previously are no longer an accurate picture of what occurs in the transmission line. Thus, the harmonic balance model becomes crucial to understanding the device physics.

We simulate using $k_{max} = s_{max} = 3$. We use the parameter-adjusting process introduced in the previous section to compare model and experiment in this device. The measured

gain at the highest applied physical power, -11.09 dBm (0.0778 mW), for signal frequencies near the pump was matched to the simulated gain at $a_{max} = 0.056$, giving a power-to-a^2 conversion factor of $0.056^2/0.0000778$=40.31.

Displayed in the top panel of Fig. 15 are the experimental gain profile at $a_{max} = 0.056$ (blue curve), along with the simulated gain profiles for $s_{max} = 3$ (green curve) and $s_{max} = 1$ (red curve). Again we observe a gain ripple that varies nearly periodically with signal frequency- see bottom left panel of Fig. 15. The frequency spacing between peaks in the gain ripple, approximately 20 MHz, corresponds to the electrical length of the transmission line, indicating that, as in Device I, the ripple is a result of reflections/ standing waves produced at the ends of the transmission line. However, the gain ripple is smaller than what we observe in Device I for equivalent gains; in Device I, the gain ripple for 9 dB peak gain has an average height of 4 dB in Device I, whereas in Device II, the gain ripple for 9 dB peak gain has an average height of 2 dB. (Note: When we state "9 dB peak gain," we mean that when the gain values are averaged to smooth the data, the peak gain in the smoothed data is 9 dB.) This illustrates that our phased-in loading technique has enabled more consistent gain performance over a wide band of frequencies. It is not unlikely that the remaining gain ripple/ phase mismatch is due to non-optimal fabrication of the impedance taper. Though the maximum gain observed is smaller in Device II (9 dB peak gain at $a_{max} = 0.056$ in Device I vs. 12 dB peak gain at $a_{max} = 0.059$ in Device II), experiments at the time of the writing of this thesis have shown that 15 dB gain with an average ripple height of 2 dB can be achieved in devices with phased-in loadings, demonstrating the higher self-oscillation threshold achieved by this technique. The reason for the lower gain is most likely the smaller pump phase length of Device II (approximately 1050 radians for Device II vs. approximately 1400 radians for Device I). The smaller the pump phase length, the smaller the self-phase shift near critical power and the smaller the gain. Nevertheless, other reasons for lower gain are possible, including non-optimal fabrication of the CPW and connectivity issues between coaxial cables and the device box.

As in Device I, two dips in gain near the pump frequency are present (bottom right panel of Fig. 15); one dip is located near 8.55 GHz, and the other is located near 8.8 GHz. The reason for these dips is the same as before: the signal or the idler falls in a stopband.

The simulated $s_{max} = 3$ gain profile is well-matched to the experimental gain profile for frequencies 6-14 GHz, with the experimental gain being significantly lower than the simulated

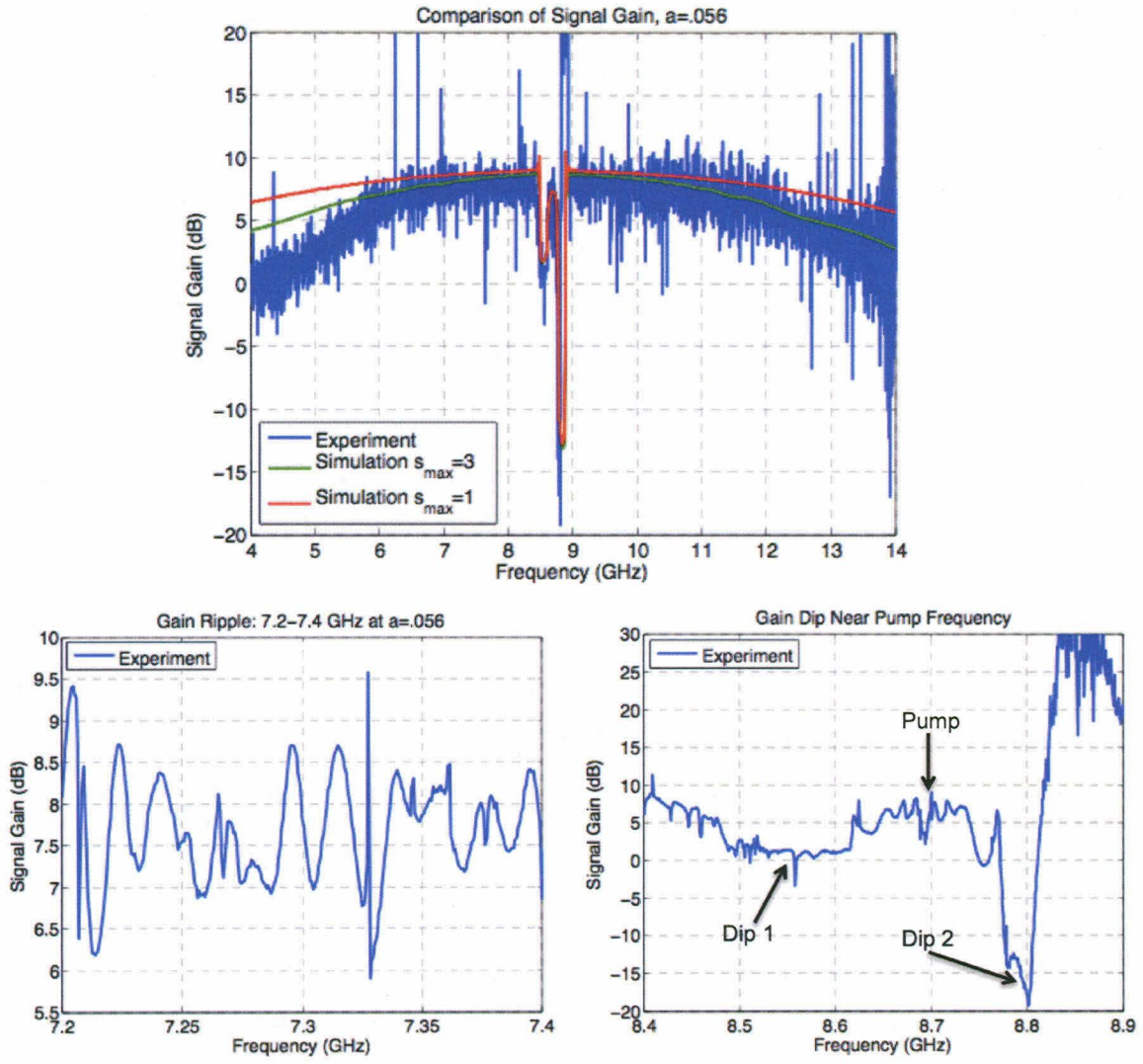

FIG. 15. **Top**: A comparison between experiment and simulation of the gain profile at power $a_{max} = 0.059$. The experimental curve is shown in blue, while the simulated curve for the $s_{max} = 3$ model is shown in green and simulated curve for the $s_{max} = 1$ model is shown in red. **Bottom Left**: A sample of the gain ripple at power $a_{max} = .056$ between 7.2 and 7.4 GHz. On average, the ripple has a height of 2 dB, with the ripple height reaching a maximum of 3.5 dB near 7.33 GHz. **Bottom Right**: The two gain dips observed near the pump frequency. Dip 1 is located near 8.55 GHz, whereas Dip 2 is near 8.8 GHz.

gain for the 4-6 GHz range. The reason for this discrepancy is unclear. However, a more significant difference exists between the $s_{max} = 1$ simulation, which only considers the signal and idler, and the $s_{max} = 3$ simulation, which considers the third harmonic sidebands. In the former profile, the signal gain and the 3 dB bandwidth is considerably larger; near the

pump, the gain in the two simulations is the same, but as we move away from the pump, the signal gain from the $s_{max} = 3$ simulation drops to 2-3 dB below the gain from the $s_{max} = 1$ simulation.

Similar to the situation in Device I, the cause of the difference in the simulated gain profiles is linked to significant power conversion from the signal photon to the ω_3 photon; given that the $s_{max} = 3$ profile is well-matched to experiment, while the $s_{max} = 1$ profile is not, it is likely that this power conversion is actually occurring in the DTWKI. In the top figure of Fig. 16, the gain of the ω_3 tone, as computed in the harmonic balance model, reaches -0.8 dB near 12.5 GHz. This corresponds to a tone whose output power is 83% of the input signal power. Given that the signal gain is less than 5 dB near 12.5 GHz, the ω_3 tone cannot be ignored.

The bottom graphic of Fig. 16 shows how the signal and ω_3 amplitudes evolve as the tones propagate down the line. Though the coupled-mode treatment was deemed to be inaccurate because of the position-dependent dispersion, equations (90) and (91), derived from an extension of the coupled-mode equations, seem to accurately reflect the numerical results. As predicted, both tones vary as sinusoids. An interesting feature of Fig. 16 not found in Fig. 11 –the corresponding result for Device I– is that at the output, both the signal and the ω_3 amplitudes are increasing. Such behavior is a result of the signal power generated from pump-to-signal conversion being larger than the signal power converted through signal-to-ω_3 conversion. The origin of the jump in the signal gain in the middle of the transmission line and the ripple in the amplitudes is unknown.

We also compare experimental results and the harmonic balance $s_{max} = 3$ model results for the gain at 7.0 GHz as a function of pump power. To account for the gain ripple, we average the gain data for the 100 MHz band centered at this frequency. Fig. 17 shows a reasonable match between model output and measurements. Note that, beyond the $a = 0.042$ data point, the experimental gain begins to slip below the simulated gain; this may be indicative of the onset of dissipation due to heating or some other effect.

Finally, we analyze the power-dependent phase of the signal. The power-dependent phase versus signal frequency for the highest pump power $a_{max} = 0.056$ is plotted in the top panel of Fig. 18, and an excellent match is obtained between simulation and experiment. As in Device I and the gain profile of Device II, the phase ripple, with peaks approximately 20 MHz apart, is likely due to reflections at the ends of the line. The bottom plot of Fig.

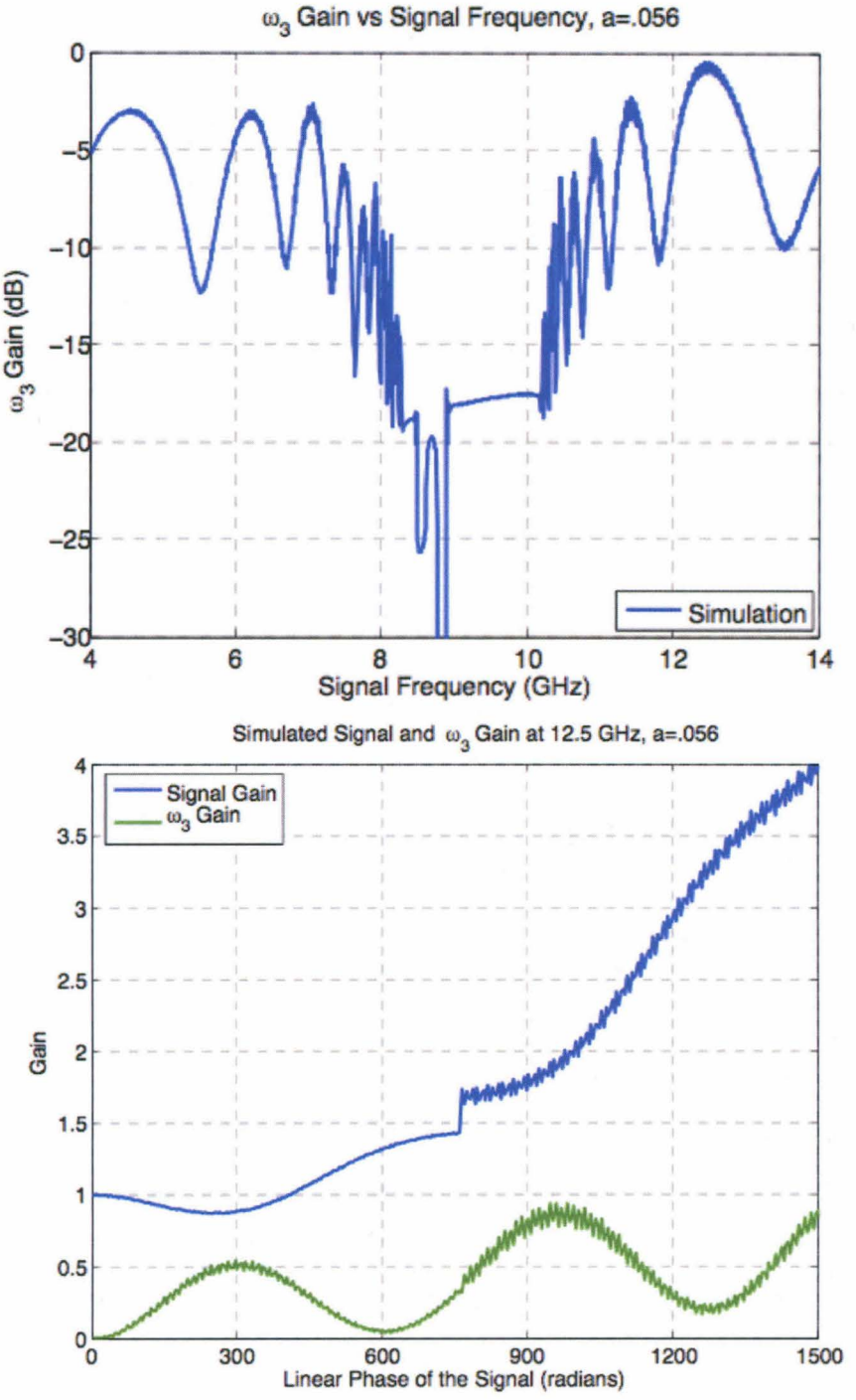

FIG. 16. **Top**: Simulated gain for the ω_3 tone. **Bottom**: Simulated signal (blue curve) and ω_3 gain (green curve) as a function of linear phase of the signal/ position for the signal frequency 12.5 GHz. As in Fig. 11, the gain units for the bottom figure are not logarithmic.

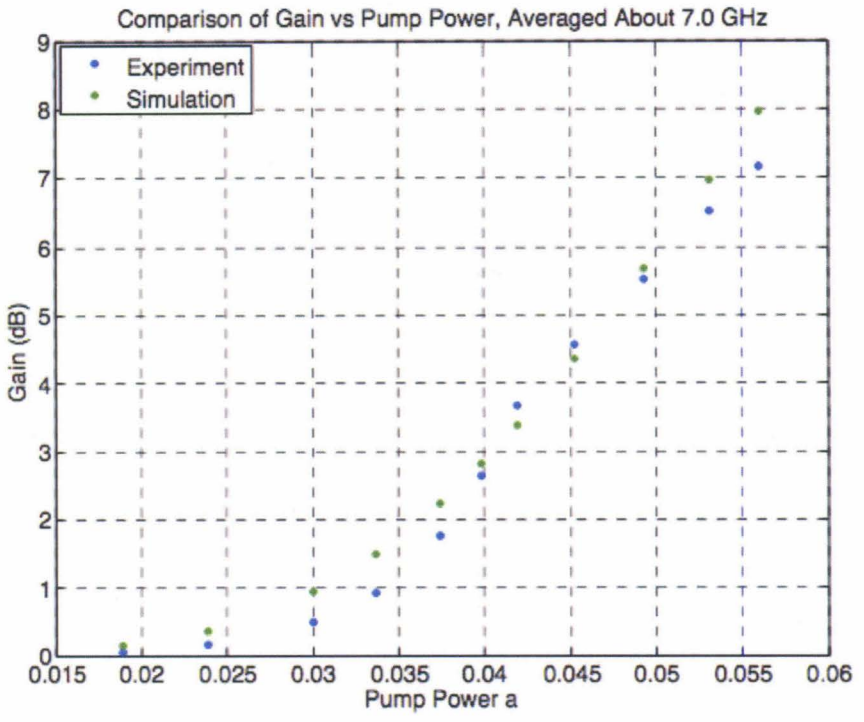

FIG. 17. Signal gain at 7.0 GHz as a function of pump power, as measured in experiment (blue curve) and computed in simulation (green curve). To account for the gain ripple, we average the gain values in the 100 MHz band centered at the signal frequency.

18 shows the power-dependent phase at 7.0 GHz as the pump power is varied; again, a reasonable match is obtained between simulation and experiment. Unlike Device I, the differences between simulation and experiment in phase values seem to be uncorrelated with the differences in gain value. (Recall that in Device I, larger discrepancies between the model and measurement are seen in both phase and gain for powers beyond $a = 0.05$ and we conclude that the phase discrepancies may be a result of dissipation.)

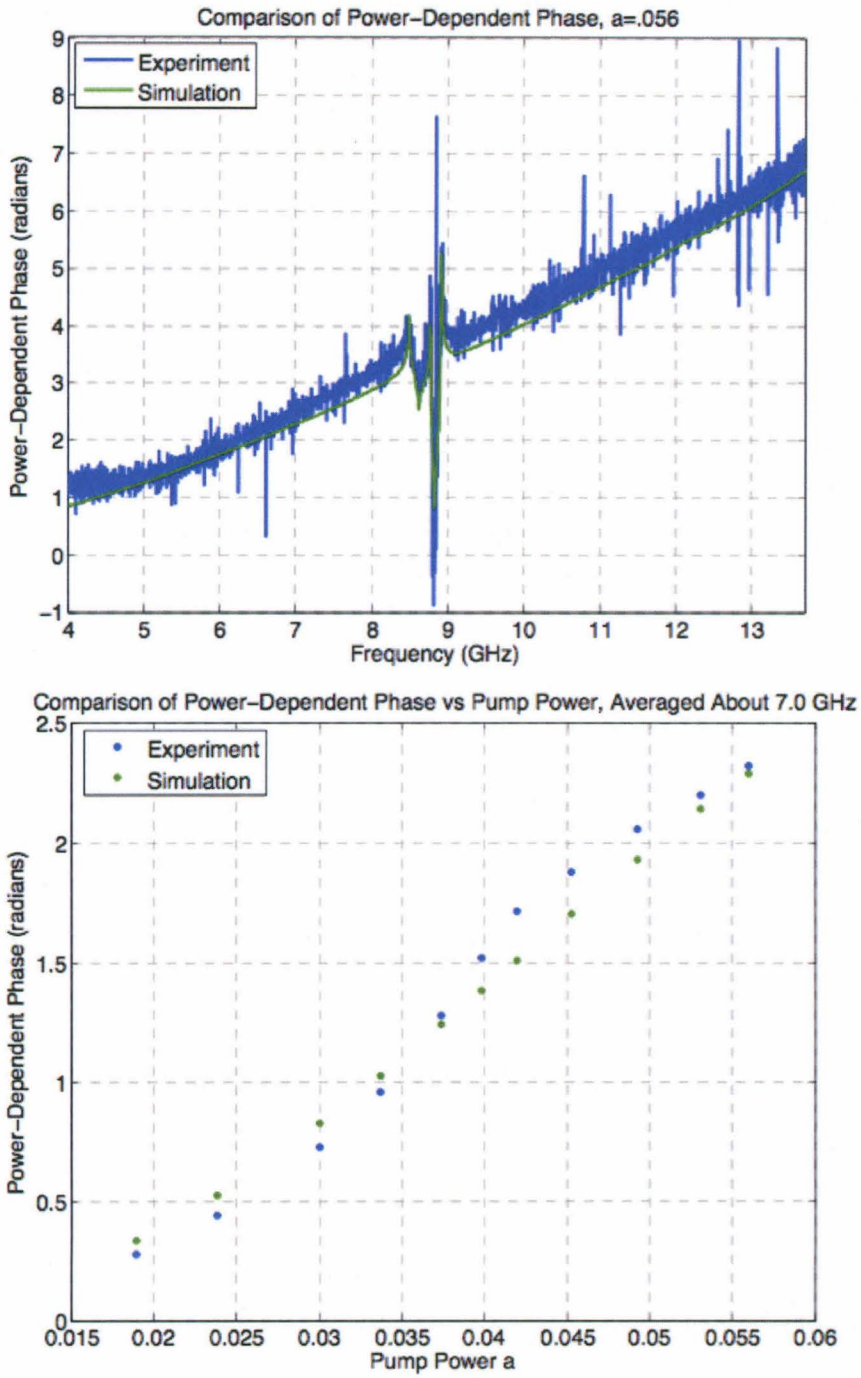

FIG. 18. **Top**: Power-dependent phase at $a_{max} = 0.056$ as a function of signal frequency, as measured in experiment (blue curve) and computed in simulation (green curve). **Bottom**: Power-dependent phase at 7.0 GHz as a function of pump power. To account for the phase ripple, we average the phase values in the 100 MHz band centered at the signal frequency.

IV. NOISE IN THE DTWKI AMPLIFIER

In this chapter, we describe the measurements performed on Device II to determine the noise the device adds during signal amplificiation. The technique used is widely known in the amplifier community as a *Y-factor measurement*, which operates as follows: Consider connecting a 50 Ω resistor, also known as a calibrator, to the input of the amplifier. In our setup, shown in Fig. 19, the calibrator is connected through a hybrid coupler to allow for introduction of the pump tone.

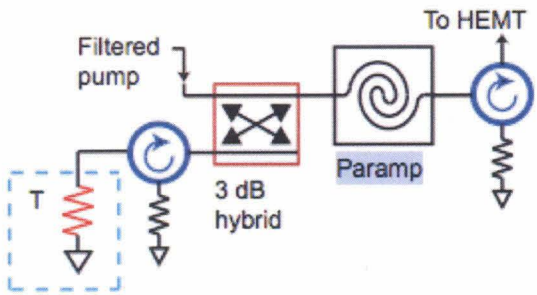

FIG. 19. A 50 Ω resistor and the filtered pump from Fig. 7 are connected to the paramp by a hybrid coupler. The resistor acts as a noise source whose noise can be adjusted by varying the temperature. The isolator between the resistor and the hybrid coupler is used to avoid heating from reflected pump power.

The noise power generated by the resistor over a signal bandwidth B centered at a frequency f is given by [12]

$$P_{cal} = B\frac{hf}{2}\coth\frac{hf}{2k_BT_R} \tag{94}$$

where T_R is the resistor temperature. B is approximately 10 Hz for these measurements. Note that in the high-temperature limit, (94) reduces to the well-known Johnson-Nyquist relation

$$P_{cal} = k_BT_RB \tag{95}$$

and in the low-temperature limit, (94) reduces to the one-half photon quantum noise:

$$P_{cal} = B\frac{hf}{2} \tag{96}$$

The hybrid coupler attenuates the calibrator noise power

$$P_{cal}^{out} = P_{cal}A_{HC} + \frac{1}{2}(1 - A_{HC}) \tag{97}$$

where A_{HC}=-3.5 $\pm$ 0.2 dB. (We have lumped the circulator attenuation into this value.) The second term represents the vacuum noise from the other input of the hybrid, used for connecting the filtered pump line. We can express P_{cal}^{out} in photon units:

$$P_{cal}^{out} = A_{cal} hf \tag{98}$$

When the pump is on, the noise power at the output of the DTWKI is

$$P_{PA,on} = G_{PA} B (A_{PA} hf + A_{cal} hf) \tag{99}$$

where G_{PA} is the paramp gain at the center frequency of the signal band and A_{PA} is the added paramp noise in photon units. As discussed in the introduction, the uncertainty principle requires $A_{PA} \geq \frac{1}{2}$ in the high gain limit. (More generally, $A_{PA} \geq \frac{1}{2}|1 - G_{PA}^{-1}|$.) The noise at the parametric amplifier output is amplified by a HEMT and additional room temperature amplifiers. The noise power at the output of this amplification stage is

$$P_{on} = Ghf B[G_{PA}(A_{PA} + A_{cal}) + A_{add}] \tag{100}$$

where G and A_{add} are the gain and added noise from these amplifiers. For convenience, we absorb the hf factors into G:

$$P_{on} = G' B[G_{PA}(A_{PA} + A_{cal}) + A_{add}] \tag{101}$$

P_{on} is measured directly in our experimental setup.

When the pump is off, the noise power at the output of the amplification stage is

$$P_{off} = G' B[A_{cal} + A_{add}] \tag{102}$$

P_{off} is also measured directly in our setup.

$G' B G_{PA}$ can be determined by changing the temperature of the 50 ohm resistor, thereby varying A_{cal}. Dividing P_{on} and P_{off} by $G' B G_{PA}$ gives

$$\frac{P_{on}}{G' B G_{PA}} = A_{PA} + A_{cal} + \frac{A_{add}}{G' B G_{PA}} \tag{103}$$

$$\frac{P_{off}}{G' B G_{PA}} = A_{cal} + \frac{A_{add}}{G' B G_{PA}} \tag{104}$$

For what follows, we will refer to the term on the left-hand side of equations (103)-(104) as *measured noise* and A_{cal} as the *calibrator noise.*

To determine the amplifier noise, we plot the measured noise vs. the calibrated noise for the pump-on and pump-off data. We then extrapolate the two lines to zero calibrator noise, $A_{cal} = 0$. Subtracting the pump-off extrapolated value from the pump-on value yields A_{PA}.

We measured the amplifier noise in two situations: (1) the pump is applied in a continuous mode, and (2) the pump is applied in a pulsed mode. When we installed the paramp in the noise measurement channel, we found that the optimal pump frequency had shifted slightly from the previous value of 8.694 GHz and was now situated at 8.689 GHz. We measured the noise at frequency f=8.314 GHz, at which the gain was G_{PA}=9.5 dB.

In the continuous mode noise measurement, the resistor temperature was set to the values 0.25 K, 0.5 K, 1 K, 1.5 K, 2.0 K, 2.5 K, 3 K, 3.5 K, and 4.0 K. The pump was turned on, and the noise at the output of the amplification stage (the stage which includes the HEMT and room temperature amplifiers) was measured at each temperature. The pump was then turned off and the noise was measured a second time. The results are shown in the top panel of Fig. 20, with the calibrator noise plotted against the measured noise. Extrapolating the pump-on and pump-off data to $A_{cal} = 0$ through a linear fit gives $A_{PA,cont} + \frac{A_{add}}{G'BG_{PA}}$=4.8 photons and $\frac{A_{add}}{G'BG_{PA}}$=2.7 photons. Subtracting the second equation from the first and propagating the uncertainty from the hybrid coupler attenuation yields an amplifier noise of $A_{PA,cont}$=2.1±0.1 photons.

In the pulsed mode noise measurement, the resistor temperature was set to 0.2 K, 0.5 K, 1 K, 1.5 K, 2.0 K, 2.5 K, 3 K, 3.5 K, and 4.0 K. The pump was turned on for 100 ms every 2 seconds (i.e. a pulsed pump), and the noise at the output of the amplification stage was measured at each temperature. The pump was then turned off and the noise was measured again. The results are shown in the bottom panel of Fig. 20. Extrapolating the pump-on and pump-off data to $A_{cal} = 0$ through a linear fit gives $A_{PA,pulse} + \frac{A_{add}}{G'BG_{PA}}$=3.9 photons and $\frac{A_{add}}{G'BG_{PA}}$=2.7 photons, yielding an amplifier noise of $A_{PA,pulse}$=1.2±0.1 photons. Thus, the pulsed mode noise performance is nearly a photon better than that of the continuous mode.

To study why the pulsed pump and continuous pump modes yield different amplifier noise values, we installed germanium thermometers on our devices and monitored the device temperature as the pump power, and consequently, the signal gain, was varied. Fig. 21, shows the result. The gain values shown are an average of the gain data for frequencies between 8.0 and 8.3 GHz. As the gain is increased from 0 to 16 dB, the device temperature

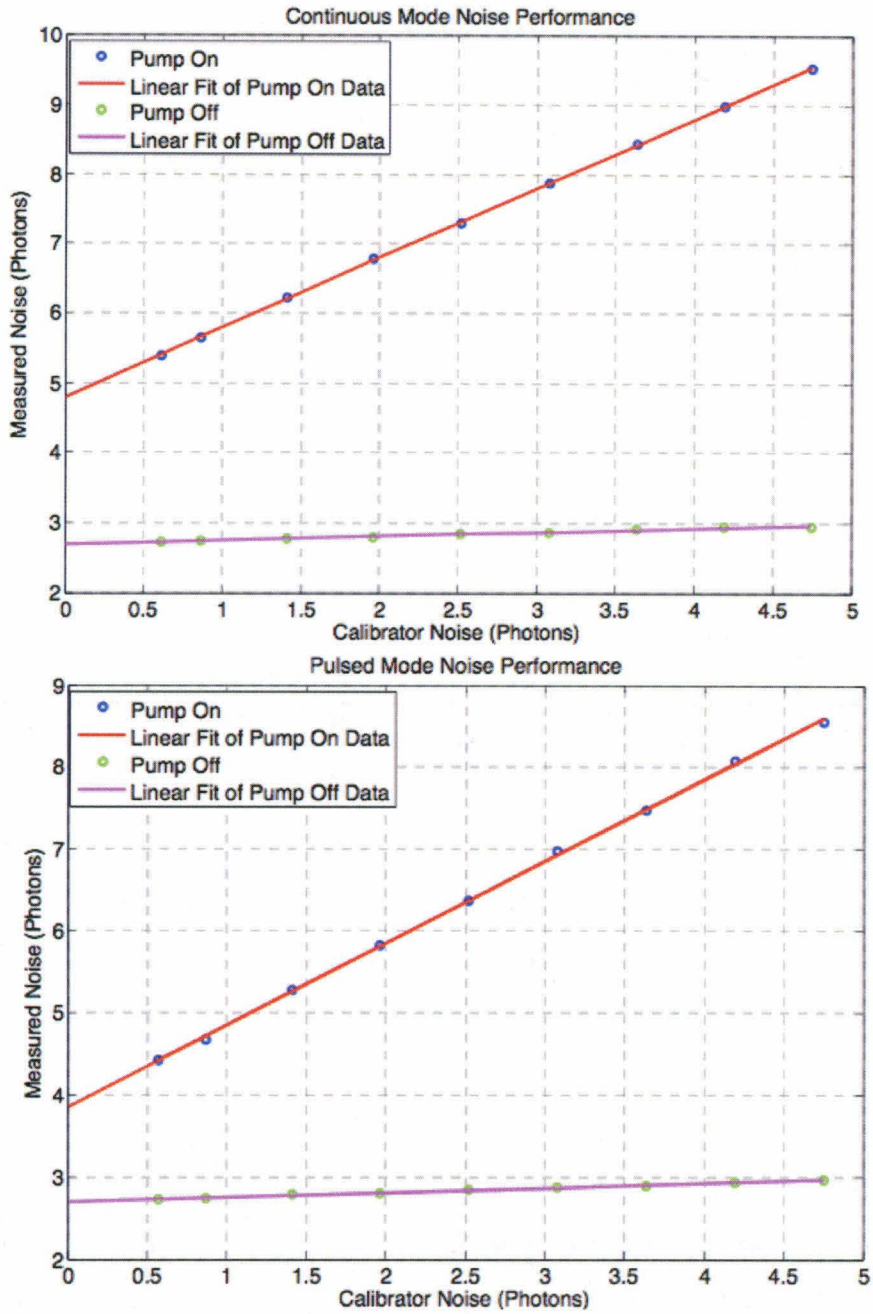

FIG. 20. **Top**: The measured noise quanta in the continuous pump mode at various temperatures/calibrator noise quanta A_{cal}. **Bottom**: The measured noise quanta in the pulsed pump mode. The pump on data points are represented in blue, and the pump off data in green. The data are fit to a line in order to extrapolate to A_{cal}=0 (red line for pump on and pink line for pump off).

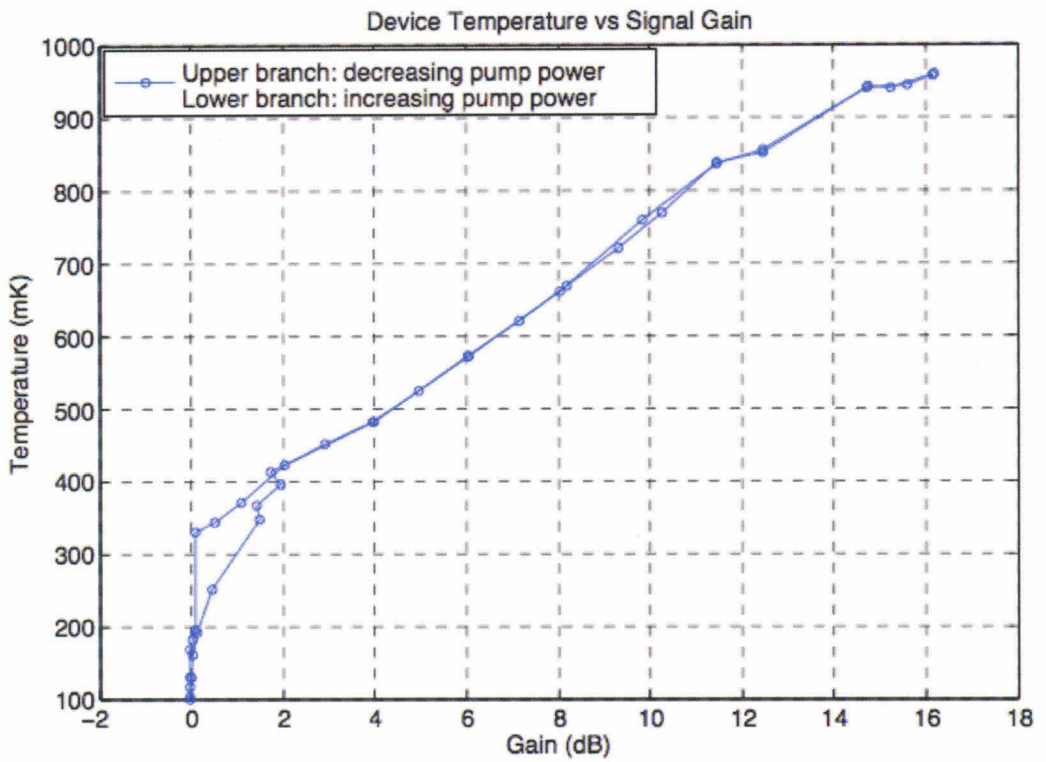

FIG. 21. The device temperature as a function of the signal gain as the pump power is increased and then decreased. The lower branch of the data represents increasing pump power, while the upper branch of the data represents decreasing pump power. Signal gain values are calculated by averaging data points between frequencies 8.0 and 8.3 GHz.

increases an order of magnitude, from 100 mK to 1000 mK. As the gain is then decreased from 16 dB to 0 dB, the device temperature decreases; however, the branch of decreasing-pump-power temperature is above the branch of increasing-pump-power temperature, with a difference of nearly 100 mK at small gain values. Both the ten-fold increase in device temperature and the temperature difference between decreasing pump power and increasing pump power sweeps are indicative of heating of the device. Thus, when the continuous pump is applied, the chip heats up, and thermal noise is generated, resulting in increased amplifier noise.

To reduce heating, we have recently begun fabricating the DTWKI devices with a gold border. In the previous generation of amplifiers, which includes Device II, heat is transported away from the device through the silicon substrate and aluminum wire bonds. Aluminum is superconducting at low temperatures, and consequently, it has low thermal conductivity

(i.e. it is not a good medium for heat conduction). Using the gold border, along with gold wirebonds between the chip and device housing, should enable better thermal management of the device and reduce noise.

V. A PROPOSAL FOR A NEW DTWKI DESIGN AND LOOKING FORWARD

Based on the data presented in Chapters 3 and 4, I propose a new design for the DTWKI with the following characteristics:

- As in Device II, we will set the center-to-center distance between loadings to 626 μm, so that the pump frequency is near 8.7 GHz. However, now we will triple the length of the device, bringing the total length close to two meters. The phase-in of the third loading will occur over 0.2 meters on each end of the filter section, while the remaining 1.6 meters in the middle of the device will maintain the third loading at one-half of the length of the first two loadings. To achieve high gain (>15 dB) with a small line length, the pump power must also be high. In turn, to get significant gain-bandwidth enhancement through phase-matching, the dispersion at the pump must be high, meaning that we must place the pump very close to the neighboring transmission stopband. As we approach the stopband, the dispersion-vs-frequency curve increases rapidly; this occurrence is illustrated in Fig. 3. Thus, there is a limited range for finding the optimal pump frequency. If we use a longer line, a lower pump power can be used to achieve high gain, meaning that not as much dispersion is necessary for phase-matching and that there is a larger range for finding the optimal pump. The lower pump power also means reduced on-chip heating and reduced thermal noise.

- Instead of using loadings of length 50 μm, 50 μm, and 25 μm in the intermediate 1.6 meters, we will use loadings of length 100 μm, 100 μm, and 50 μm. At each end of the line, the first three loadings are all 100 μm in length. As we approach the middle of the line, every third loading is gradually reduced in length from 100 μm to 50 μm; this reduction in length, as mentioned before, occurs over 0.2 meters at each end of the line. By increasing the length of the loading, we make the third stopband feature wider, and therefore, the ω_3 tone can be ignored for a larger range of signal frequencies. This results in higher gain and higher bandwidth.

- Currently, the NbTiN thin films are grown on a silicon substrate. We will substitute sapphire for silicon. At low temperatures, sapphire has a higher thermal conductivity than silicon, meaning that sapphire will better limit on-chip heating. The sapphire will complement the gold-plating discussed in the previous chapter.

Estimates based on the harmonic balance model and recent experiments indicate that such an amplifier should operate with an added noise of at most 1 photon and should readily achieve more than 20 dB gain with a 3 dB bandwidth of more than 2 GHz on each side of the pump.

DTWKI amplifier development is progressing on all fronts. Recently, we have discovered that the signal fluctuations are indeed highly correlated with idler fluctuations, though probably not at the level of a two-mode-squeezed state. Our colleagues Kent Irwin, Jiansong Gao, Dave Pappas, and Mike Vissers at NIST Boulder have demonstrated 8 dB gain in DTWKI amplifiers using titanium nitride thin films. TiN exhibits a maximum inductance nonlinearity comparable to that found in NbTiN; however, the pump power at which the maximum nonlinearity is achieved is two orders of magnitude lower in TiN than in NbTiN. Previously, the Caltech/JPL development group had not been able to demonstrate gain in DTWKI devices using TiN. The exciting result at NIST could lead not only to a diversification of the types of superconducting material used, but also to a further reduction of noise.

Our group is also developing amplifiers that are not based on the nonlinear kinetic inductance of superconducting thin film nitrides. One disadvantage of thin films is that they possess a low inductance nonlinearity compared to Josephson junctions, in which nonlinearities of 20-25% can be achieved. However, parametric amplifiers based on Josephson junctions have not demonstrated a dynamic range as large as that for amplifiers based on thin films. Is there a material for which we can achieve inductance nonlinearities higher than thin films while still achieving dynamic range larger than that for Josephson parametric amplifiers? Experiments performed by graduate student Aditya Kher show that NbTiN nanowires might do the trick. He is currently developing resonant paramps based on nanowires. A traveling-wave amplifier based on a low-pass LC ladder network, in which the lumped inductances are replaced by nanowires, is also being designed.

VI. APPENDIX

A. Computation of Jacobian for Harmonic Balance Model

Here, we compute the Jacobian of size $4Nk_{max} \times 4Nk_{max}$,

$$\tilde{J} = \frac{\partial \tilde{\underline{\mathbf{c}}}}{\partial \tilde{\mathbf{a}}} \tag{105}$$

It is clear that the problem of computing the Jacobian reduces to computing, for each transmission line section, the four derivatives $\frac{\partial \underline{c}_1(n\omega_p)}{\partial a_1(r\omega_p)}$, $\frac{\partial \underline{c}_1(n\omega_p)}{\partial a_2(r\omega_p)}$, $\frac{\partial \underline{c}_2(n\omega_p)}{\partial a_1(r\omega_p)}$, and $\frac{\partial \underline{c}_2(n\omega_p)}{\partial a_1(r\omega_p)}$ for any r, $-k_{max} \leq r \leq k_{max}$, and any n, $1 \leq n \leq k_{max}$. These derivatives are easily computed using (32) and (33):

$$\begin{aligned}
\frac{\partial \underline{c}_1(n\omega_p)}{\partial a_1(r\omega_p)} = \frac{ink_pL}{8I_*^2 Z_c} e^{-ink_pL} [& \sum_{k,l} \delta_{n,k+l+r} [(1-\delta_{k,r})(1-\delta_{l,r}) a_1(k\omega_p) a_1(l\omega_p) \mathrm{sinc}(nk_pL) \\
& - 2(1-\delta_{l,r}) a_1(l\omega_p) a_2(k\omega_p) \mathrm{sinc}((n-k)k_pL) \\
& + a_2(k\omega_p) a_2(l\omega_p) \mathrm{sinc}(rk_pL)] \\
& + \sum_{k} \delta_{n,k+2r} [2(1-\delta_{k,r}) a_1(k\omega_p) a_1(r\omega_p) \mathrm{sinc}(nk_pL) \\
& - 2a_1(r\omega_p) a_2(k\omega_p) \mathrm{sinc}((n-k)k_pL)] \\
& + \delta_{n,3r} (a_1(r\omega_p))^2 \mathrm{sinc}(nk_pL)]
\end{aligned} \tag{106}$$

$$\begin{aligned}
\frac{\partial \underline{c}_1(n\omega_p)}{\partial a_2(r\omega_p)} = \frac{ink_pL}{8I_*^2 Z_c} e^{-ink_pL} [& \sum_{k,l} \delta_{n,k+l+r} [-a_1(k\omega_p) a_1(l\omega_p) \mathrm{sinc}((n-r)k_pL) \\
& + 2(1-\delta_{l,r}) a_1(k\omega_p) a_2(l\omega_p) \mathrm{sinc}(kk_pL) \\
& - 2(1-\delta_{k,r})(1-\delta_{l,r}) a_2(k\omega_p) a_2(l\omega_p)] \\
& + \sum_{k} \delta_{n,k+2r} [2a_1(k\omega_p) a_2(r\omega_p) \mathrm{sinc}(kk_pL) \\
& - 2(1-\delta_{k,r}) a_2(k\omega_p) a_2(r\omega_p)] \\
& - \delta_{n,3r} (a_2(r\omega_p))^2]
\end{aligned} \tag{107}$$

$$\frac{\partial \underline{c}_2(n\omega_p)}{\partial a_1(r\omega_p)} = -\frac{ink_pL}{8I_*^2 Z_c} e^{-ink_pL} [\sum_{k,l} \delta_{n,k+l+r} [(1-\delta_{k,r})(1-\delta_{l,r}) a_1(k\omega_p) a_1(l\omega_p)$$

$$
\begin{aligned}
&- 2(1-\delta_{l,r})a_1(l\omega_p)a_2(k\omega_p)\mathrm{sinc}(kk_pL) \\
&+ a_2(k\omega_p)a_2(l\omega_p)\mathrm{sinc}((n-r)k_pL)] \\
&+ \sum_k \delta_{n,k+2r}[2(1-\delta_{k,r})a_1(k\omega_p)a_1(r\omega_p) \\
&- 2a_1(r\omega_p)a_2(k\omega_p)\mathrm{sinc}(kk_pL)] \\
&+ \delta_{n,3r}(a_1(r\omega_p))^2] \qquad (108)
\end{aligned}
$$

$$
\begin{aligned}
\frac{\partial \underline{c}_2(n\omega_p)}{\partial a_2(r\omega_p)} = -\frac{ink_pL}{8I_*^2Z_c}e^{-ink_pL}[&\sum_{k,l}\delta_{n,k+l+r}[-a_1(k\omega_p)a_1(l\omega_p)\mathrm{sinc}(rk_pL) \\
&+ 2(1-\delta_{l,r})a_1(k\omega_p)a_2(l\omega_p)\mathrm{sinc}((n-k)k_pL) \\
&- (1-\delta_{k,r})(1-\delta_{l,r})a_2(k\omega_p)a_2(l\omega_p)\mathrm{sinc}(nk_pL)] \\
&+ \sum_k \delta_{n,k+2r}[2a_1(k\omega_p)a_2(r\omega_p)\mathrm{sinc}((n-k)k_pL) \\
&- 2(1-\delta_{l,r})a_2(k\omega_p)a_2(r\omega_p)\mathrm{sinc}(nk_pL)] \\
&- \delta_{n,3r}(a_2(r\omega_p))^2\mathrm{sinc}(nk_pL)] \qquad (109)
\end{aligned}
$$

The Jacobian can then be constructed by evaluating these derivatives at the value of $\tilde{\mathbf{a}}$ found in step 3 or step 6 of the iterative process and entering them at the appropriate locations in a $4Nk_{max} \times 4Nk_{max}$ matrix, the appropriate locations being determined by the manner in which we ordered the entries of $\underline{\tilde{\mathbf{c}}}$ and $\tilde{\mathbf{a}}$.

[1] Eom et al. A wideband, low-noise superconducting amplifier with high dynamic range. *Nature Physics* 8, 623-627, 2012.

[2] R. H. Parmenter. Nonlinear electrodynamics of superconductors with a very small coherence distance. *RCA Review*, 23:323-352, 1962.

[3] Leduc et al. Titanium nitride for ultrasensitive microresonator detectors. *Applied Physics Letters* 97, 102509, 2010.

[4] R. Landauer. Shock waves in nonlinear transmission lines and their effect on on parametric amplification. *IBM J. Res. Dev.*, 4(4):391-401, 1960.

[5] W.H. Louisell, A. Yariv, and A.E. Siegman. Quantum Fluctuations and Noise in Parametric Processes. I. *Physical Review*, 124:1646-1654, Dec 1961.

[6] M. A. Castellanos-Beltran, et al. Amplification and squeezing of quantum noise with a tunable Josephson metamaterial. *Nature Physics*, 4:929-931, Dec 2008.

[7] Tholen et al. Nonlinearities and parametric amplification in superconducting coplanar waveguide resonators. *Appl. Phys. Lett.*, 90(25), Jun 18 2007.

[8] Richard L. Garwin, Wilton A. Hardy, and Rolf W. Landauer. Optical traveling wave parametric devices. U. S. Patent Number 3297875, Jan 1967.

[9] G.P. Agarwal. *Applications of nonlinear fiber optics* (ed Agrawal, G. P.) (2001).

[10] R. Stolen and J. Bjorkholm. Parametric amplification and frequency conversion in optical fibers. *IEEE J. Quantum Electron.* 18, 1062 1072. ISSN: 0018-9197 (1982).

[11] J. A. Tucker and M. J. Feldman. Quantum detection at millimeter wavelengths. *Rev. Mod. Phys.*, 57(4):1055-1114, 1985.

[12] Clerk et al. Introduction to Quantum Noise, Measurement, and Amplification. *ArXiv e-prints.* arXiv:0810.4729v2 [cond-mat.mes-hall] (Apr. 2010).